Results in Engineering 28 (2025) 107992

Contents lists available at ScienceDirect

Results in Engineering

journal homepage: www.sciencedirect.com/journal/results-in-engineering

A low-temperature hydrothermal approach to fabricate bactericidal nanostructures on 3D-printed polylactic acid surfaces against *Pseudomonas aeruginosa* bacteria

S.P.S.N.Buddhika Sampath Kumara [a,b,c], Preetha Ebenezer [a,b], S.W.M.Amal Ishantha Senevirathne [a,b], Mohammad Mirkhalaf [a,b], Prasad K.D.V. Yarlagadda [c,d], Laura J. Bray [a,b,*], Asha Mathew [d,*]

[a] School of Mechanical, Medical and Process Engineering, Faculty of Engineering, Queensland University of Technology (QUT), Brisbane, QLD, 4000, Australia
[b] Centre for Biomedical Technologies, Queensland University of Technology (QUT), Brisbane, QLD 4000, Australia
[c] Australian Research Council Training Centre for Multiscale 3D Imaging, Modelling, and Manufacturing, Queensland University of Technology (QUT), Brisbane, QLD 4000, Australia
[d] School of Engineering, University of Southern Queensland, Springfield, QLD 4300, Australia

ARTICLE INFO

Keywords:
Antibacterial
Antimicrobial
Nano-topographies
PLA
3D printing

ABSTRACT

Surface modification offers the opportunity to create nano-topographies on various materials. Such modifications are widely applied to enhance solar energy absorption and electromagnetic shielding. An additional high-impact application involves nano-topographic surfaces designed to combat biofilm formation by nature inspired surfaces, such as cicada and dragonfly wings, which physically lyse bacterial cells. Such mechano-bactericidal surfaces have attracted growing interest over the past decade, and ongoing efforts translate these structures into medical and industrial applications. While considerable progress has been achieved with metallic and ceramic surfaces, advancements in polymers remain limited, despite their widespread use. In this study, a low-temperature hydrothermal approach successfully modified the 3D-printed polylactic acid (PLA) surface to nano-topographies. Although the literature describes a limited number of strategies for producing nanostructures on 3D metallic surfaces, fabricating such structures on 3D polymeric surfaces remains challenging using conventional methods. This study demonstrates the successful fabrication of distinct nanostructures on both the top and bottom surfaces of a 3D-printed PLA substrate. The produced surfaces were characterised via scanning electron microscopy (SEM), atomic force microscopy (AFM), SEM-Energy Dispersive Spectroscopy (EDS), X-ray Photoelectron Spectroscopy (XPS), and Fourier-transform infrared spectroscopy (FTIR). The bactericidal efficacy (BE) was quantified via LIVE/DEAD™ BacLight™ bacterial viability assay with inverted fluorescence microscopy images. Among the developed structures, Nano-Pockets with an average pore diameter of ~275 nm exhibited the highest BE, achieving a 48.8 % reduction in Gram-negative *Pseudomonas aeruginosa* viability within 1 hour of incubation. This approach, therefore, lays the foundation for fabricating nanostructures on 3D-printed polymeric surfaces with complex geometries.

1. Introduction

Antifouling surfaces are increasingly important due to their role in preventing biofilm formation on various applications such as biomedical implants and devices (BIDs) [1,2], marine vessels (e.g. ship hulls) [3,4], heat exchangers [5,6], aircraft fuel systems [7–9], pipelines (specially in food processing and water distribution) [10–12], bioreactors and fermentation systems [13,14], surgical instruments [15,16], and steel infrastructures (e.g. Bridges) [17,18]. Microorganisms, such as bacteria, adhere to solid surfaces and secrete extracellular polymeric substances (EPS), which leads to the formation of biofilms [2,19]. These biofilms compromise the functionality of the applications. For instance, bacterial colonization on biomedical implants can cause infection and implant failure, potentially resulting in fatalities or revision surgeries [2,20–22]. On the other hand, biofilms on marine surfaces increase fuel consumption, frictional resistance, and greenhouse gas emissions [4,23,24].

* Corresponding authors.
E-mail addresses: laura.bray@qut.edu.au (L.J. Bray), asha.mathew@unisq.edu.au (A. Mathew).

https://doi.org/10.1016/j.rineng.2025.107992
Received 11 July 2025; Received in revised form 11 October 2025; Accepted 30 October 2025
Available online 31 October 2025

Additionally, microbial contamination of fuel leads to biofilm formation, clogging aircraft fuel filters and resulting in corrosion and failure of fuel control systems, which poses a significant safety risk [8,9,25].

BIDs are among the fastest-growing applications and failures have long been a significant issue in the health care sector [26]. According to various research predictions, the global biomedical implant market is expected to grow at a compound annual rate of 6.8–9.0 % from 2023 to 2032 [25–28].

However, several factors have led these BIDs to fail such as biomechanical failure, bacterial infections (biofilm formation), osseointegration failure, and damage to nerves or tissues [22,27]. Bacterial infections on BIDs is a critical issue which needs more attention due to its consequences such as amputation, revision surgeries, antibiotic resistants, superbug formation, high health care cost, and mortality [2,20,21].

However, the physical removal of bacterial biofilms by mechanical debridement is inefficient, expensive, and time consuming. Different antimicrobial approaches have been carried out in the literature to mitigate bacterial colonisation. These approaches include the use of antibiotics, coatings (metal ions, metal and metallic oxide nanoparticles, 2D nanomaterials, hydrophilic polymers, biomolecules (antimicrobial peptides and chitosan)), and antimicrobial nanostructured surfaces [2, 28,29]. While antibiotics are widely used in biomedical applications, their repeated and prolonged use increases the risk of antimicrobial resistance (AMR) and the emergence of superbugs [30,31].According to the research predictions, misuse of antibiotics in healthcare, animal health, and agriculture accelerates the spread of resistance genes, fuelling a "Silent Pandemic" that may become the leading cause of death by 2050 and this will also leads to a loss of global annual gross domestic production by 3.8 % [32,33].

The use of antimicrobial nanoparticles such as coating on surfaces has been an excellent solution with high bactericidal activity to combat against bacterial infections [34]; However, according to the biomedical context, exceeding a certain dose limit can cause inflammatory responses due to DNA damage to human cells via the oxidative stress caused by reactive oxygen species (ROS) [2,29,35,36]. The discovery of antimicrobial natural nanostructured surfaces from cicada wings, dragonfly wings, damselfly wings, gecko skin, shark skin, taro leaf, and lotus leaf have made a significant impact on the development of artificial antibacterial nanostructured surfaces [2,37–40]. These surfaces kill the bacteria due to prolonged stress produced from the sharp nano-features via piercing or rupturing the bacterial cell membrane and this killing mechanism is identified as mechano-bactericidal activity [41,42]. In addition to rupturing bacterial cells, the ability of hydrophobic nanopatterned surfaces to repel bacteria is a critical factor in preventing adhesion and biofouling [43–45]. Overall, nanostructures exhibit a wide range of functional properties and applications, particularly in relation to their antibacterial activity, as illustrated in Fig. 1.

Many processes have been used to fabricate these bioinspired antibacterial nanostructured surfaces on polymers via Nanoimprinting Lithography (NIL) [46,47], Laser based Lithography (LL) [48,49], Electron Beam Lithography (EBL) [50,51], Anodic Aluminum Oxide Template (AAOT) [52,53], Reactive Ion Etching (RIE) [40,54,55], Colloidal Lithography (CL) [37,39], Wet etching [56]. Interestingly, to produce these nanostructures effectively on different materials, many researchers have used a combination of these processes [49], making the process more complex and less cost effective. Imprinting techniques such as NIL, and some lithography techniques such as EBL and LL, have been used to develop these nano-features on polymer materials [2]. However, disadvantages such as non-facile, slow fabrication, and damage of nano-features during the demoulding makes these processes challenging and inefficient [2]. Also, scalability is one of the most important factors, which is challenging in these processes. The majority of these antibacterial nanostructured surface developments were on metals and ceramics due the ease of fabrication at high temperature and high-pressure conditions without damaging the bulk material [2]. For instance, TiO_2 nanowires were developed on a titanium alloy surface via a chemical synthesis process called hydrothermal synthesis where it requires a pressure vessel to react at high temperature and high-pressure conditions [57–60]. Moreover, among these fabrications, hydrothermal synthesis is able to fabricate antibacterial nanostructures on three-dimensional (3D) metallic surfaces while other techniques have succeeded in producing high bactericidal nanostructures on two-dimensional (2D) flat surfaces on metals, ceramics and polymers [58,60,61].

With the advantages of high 3D printability, high biocompatibility, biodegradability, low density, and corrosion resistivity, polymers play a key role specially in producing patient specific BIDs [2,62,63] with internal and external geometries and other applications such as antifouling surfaces [64] and antireflection surfaces [65]. 3D printing has become one of the highly used manufacturing processes for patient specific BIDs due to low cost, less lead time, low material waste, net shape manufacturing, low part weight, and rapid production from a CAD model [62,66–68]. Interestingly, Shi et al. was able to fabricate 3D printed polymeric materials with nanostructures via photo-polymerization induced microphase separation method and unable to test these surfaces its antibacterial activity [69]. Patil et al. was able to

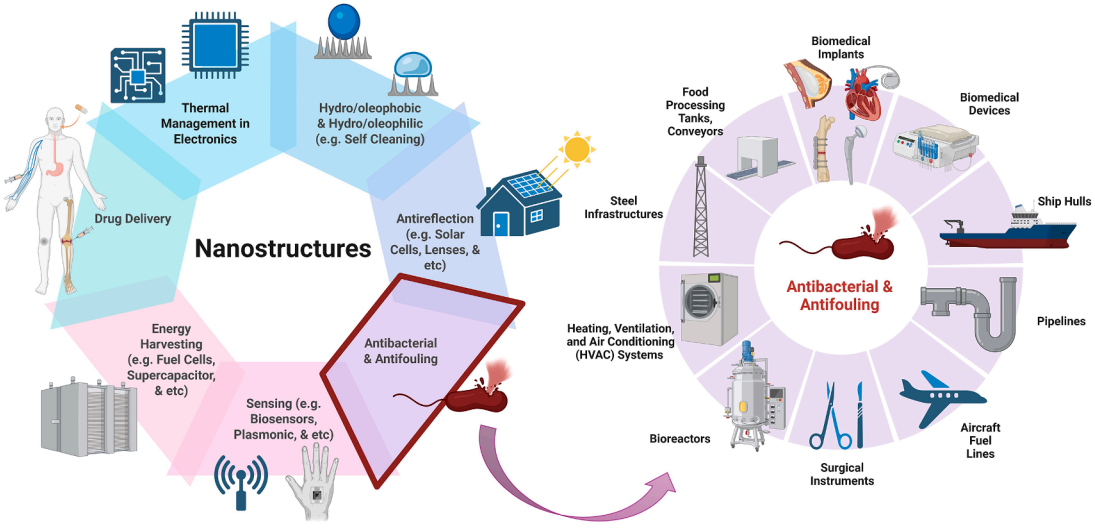

Fig. 1. Functional properties and range of applications with regards to the antibacterial and antifouling characteristics of nanostructures (Created in BioRender. Sinhasana, B. (2025) https://BioRender.com/b33e1mc).

fabricate antibacterial nanostructured surfaces against *P. aeruginosa* bacteria via reactive ion etching approach on nitrile glove surfaces with the aim of bactericide surgical nitrile gloves [70]. However, the experimental study was based on 2D flat nitrile surfaces hinders the effectivity them on 3D surfaces. Moreover, Yoo et al. was able to develop a method to fabricate ZnO nanowires on flexible polymer substrates (Polyethylene terephthalate (PET), Polyimide (PI) and Polycarbonate (PC)) via a low temperature hydrothermal approach by seeding ZnO [71]. Yet this approach was not tested for bactericidal activity and wasn't able to develop the same nanostructures on 3D polymeric surfaces without seeding metallic oxides. In conclusion, producing bactericidal nanostructured surfaces on polymeric 3D surfaces have not yet been achieved. This research gap extends beyond biomedical applications and is relevant to a wide range of areas, as shown in Fig. 1.

Hydrothermal synthesis is a successful process for producing bactericidal nanostructures on metallic 2D and 3D surfaces [58,72]. However, producing these nano-features on polymeric surfaces is a challenging task due to low melting temperature and glass transition temperature (GTT) of polymers [2]. Often, hydrothermal conditions will warp the polymer surface and change the mechanical properties due to thermal and hydrolytic degradation [73,74]. However, use of this hydrothermal process under low temperature, controlled alkaline concentration and reaction time will enable paths to fabricate bactericidal polymeric nanostructures [74]. A similar approach was studied by Yoo et al. to produce ZnO nanowires on polymeric flat surfaces via low temperature (70 °C for PET and 90 °C for PI and PC) hydrothermal process [71]. However, use of this hydrothermal process for pure polymeric surface modifications are yet unmet.

To address these research gaps we have used a novel approach to produce nanostructures via a low-temperature hydrothermal treatment to physically modify the surface of 3D printed PLA. This process includes both hydrolysing and nucleation approach with use of a saturated solution from alkaline degraded PLA as the precursor solution. PLA was selected for this study due to its high biocompatibility and biodegradability in biomedical context, as well as its widespread use as a 3D printing polymer [75–78].

2. Experimental methods

2.1. Materials

PLA filaments with a diameter of 1.75 mm were obtained from RS components Pty Ltd, Australia. PLA substrates were 3D printed via Lulzbot mini 2 fused deposition modelling (FDM) printer (0.25 mm layer thickness). Size of the 3D printed PLA substrate size was 10 mm X 8 mm X 1.5 mm (L x W x H). NaOH pellets (>97 % assay) were purchased from ProSciTech Pty. Ltd, Australia. Ethanol (99.5 % v/v) was purchased from Ajax Finechem, Australia. Nutrient broth powder and Phosphate-buffered Saline (PBS) were purchased from Oxoid, USA.

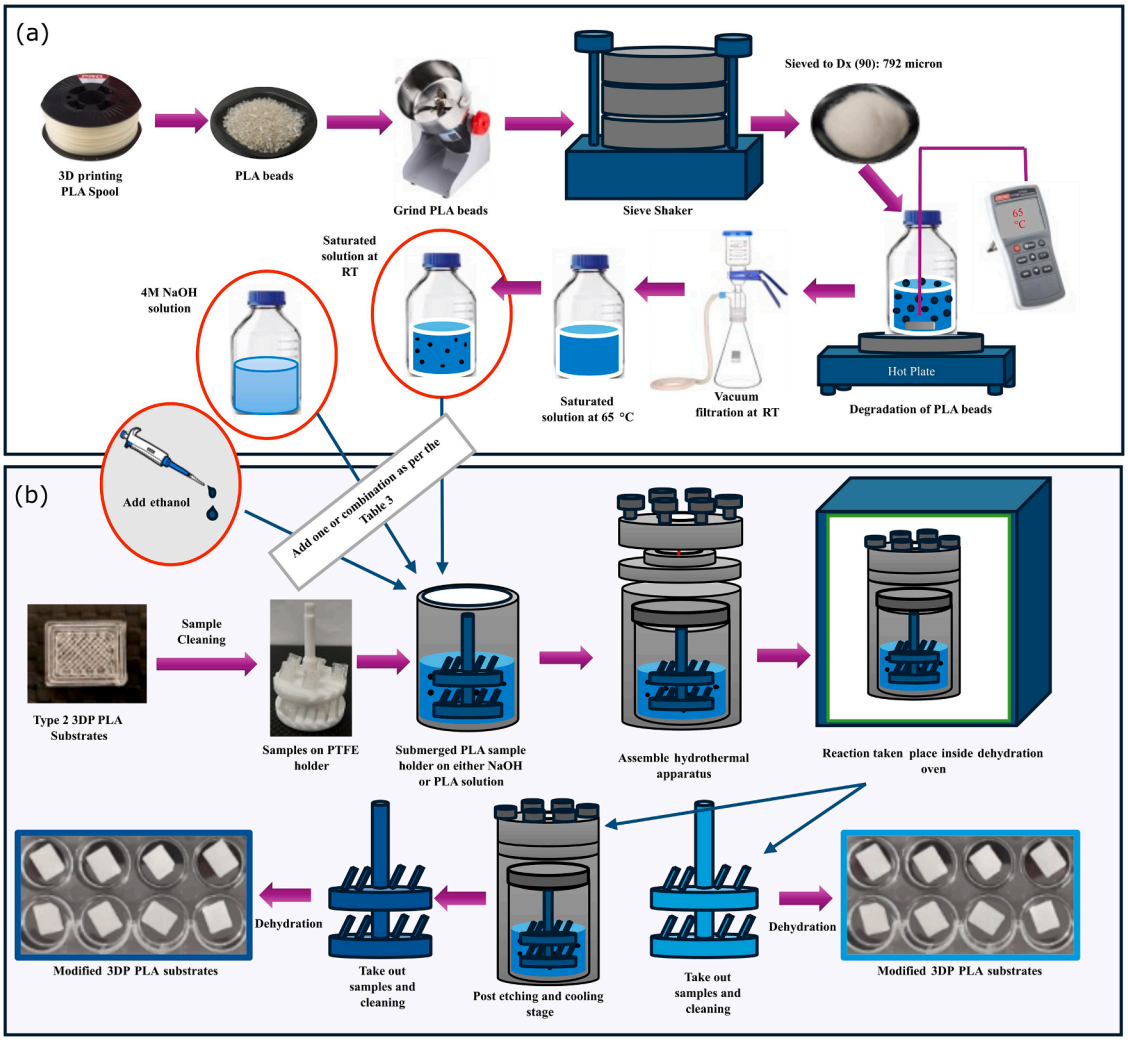

Fig. 2. a) PLA solution preparation process from grinded 3D printing PLA spool filaments; b) Surface modification process via the low-temperature hydrothermal approach.

2.2. Nanofabrication

For the low-temperature hydrothermal process, NaOH solution was prepared using NaOH pellets (7.2 g for 3 M, 9.6 g for 4 M, and 12 g for 5 M) in a 60 ml of milliQ DI water (18.2 MΩ.cm at 22.5 °C via Millipore Q-pod milliQ water system) via sonicating inside the water bath sonicator for 7 min at RT. 3D printing PLA spool was grinded using a 3200 W high speed multi-function comminutor, sieved to a range of Dx (90): 750–830 μm size granules (see **Figure S1, Figure S2**, and **Table S2**) and added to the prepared NaOH solution (3 M, 4 M or 5 M). The solution was stirred using a magnetic stirring bead to 200 rpm at 65 °C (measured using (RS PRO 1319A Wired Digital Thermometer and RS PRO Type K Thermocouple 1 m Length, 1.5 mm Diameter) as shown in Fig. 2(a) until the solution turned saturated from the degraded products of PLA. 11.85 g, 16.8 g, and 20.4 g of PLA granules was required to saturate 3 M, 4 M, and 5 M NaOH solutions with degraded products of PLA. To ensure there is sufficient PLA granules for the reaction, 23 g was added to each solution with different NaOH concentrations (3 M, 4 M or 5 M). The PLA solution underwent vacuum filtration using 0.8 μm cellulose filter paper after different time intervals, and the weight of the filtered wet PLA was measured until a constant filtered weight was attained. The average of this consistent weight was taken to calculate saturated weight of PLA using Eq. (1) while Eq. (2) was used to calculate the PLA concentration. The $t_{4/65}$ value was taken as the starting time of getting consistent filtered PLA weight.

$$\textit{Saturated PLA weight}\ (mg) = \textit{Weight of initially added PLA powder}\ (mg) - \textit{Filtered wet weight of PLA powder after saturation}\ (mg) \quad (1)$$

$$\textit{Saturated Concentration of degraded products of PLA} = \frac{\textit{Saturated PLA weight}\ (mg)}{\textit{DI water volume}\ (ml)} \quad (2)$$

A 60 ml volume of prepared saturated PLA solution was measured using a measuring cylinder and transferred to the Teflon container in the hydrothermal vessel (Parr acid digestion vessel: capacity 125 ml) as shown in the Fig. 2(b). Simultaneously, A total of 10 3D printed PLA substrates underwent a thorough cleaning process involving 3-step cleaning procedure for both sides of the substrate: (1) 99.5 % v/v ethanol, (2) milliQ DI water, and (3) N_2 gas. The cleaned samples were then attached to the Teflon holder at an angle of 45° (Fig. 2(b)). Then the holder with PLA substrates were inserted into the PTFE vessel. To increase the pressure slightly above the atmospheric pressure of 1 bar, 300 and 600 μl of 99.5 % v/v ethanol was added into the solution. The reactions were conducted at a temperatures of 22.5 (RT: room temperature), 80, and 90 °C, which was the designated oven setting.

The in-situ temperature monitoring is carried out using a K type thermocouple fixed to the Teflon container inside the hydrothermal vessel. Hydrothermal reaction was taken place for different time intervals such as 2, 2.5, and 3 h. Then the vessel was taken out from the oven and kept inside the fume hood for cooling and further reaction for 22 h for all the experiments except Exp. A. Finally, samples were taken out from the vessel and cleaned the samples again following the 3-step cleaning procedure to remove chemical residues on the surface. To remove trapped ethanol and moisture inside the sample, all the samples were dehydrated inside a dehydration oven for 3 h at 40 °C.

2.3. Nano-topography characterisations

To study the surface topography for identifying and quantifying the nano-features, SEM and AFM were used. For SEM imaging, samples were attached to the SEM stubs using both carbon tape and a carbon coating. Applying carbon coating reduced the polymer sample drifting due to its non-conductive characteristic. Samples were coated with a 10 nm gold layer and characterised with a control sample using the TESCAN Mira 3 SEM instrument. Bruker AFM was used to characterize the surface deviation of the treated PLA substrates. OLTESPA-R3 (material: 0.01–0.02 ohm-cm silicon) with tapping mode was used. A 5 μm scan size and 256 histogram bins were used. Each sample was scanned in 3 different locations. Due to the high deviation of surface in 3D printing, 1st order plane fit and 1st order flatten option was used to make the surface fit to the horizontal plane for assessing the roughness results. Nikon ECLIPSE LV100N Polarised light microscopy was used to image 3D printed PLA samples to analyse the material deposition by using 40X objective. To identify the chemical composition of the surfaces, XPS (Kratos AXIS Supra) was used. Al K alfa x-ray source was used to collect survey spectra (3 distinct locations) of samples. SEM-EDS (TESCAN Mira3) was used to identify the element distribution on the treated surface. SE and EDS images were compared, and EDS point analysis was used due to low accuracy in EDS mapping on 3D printed polymer samples (non-conductive, non-flat, and porous). To analyse the changes in functional groups following the treatment, FTIR spectroscopy was performed using a Nicolet FTIR instrument equipped with a VariGATR germanium ATR accessory. Spectra were obtained by co-adding 256 scans at a resolution of 4 cm^{-1}. The resulting data were ATR-corrected and presented as absorbance spectra.

2.4. Compression tests

The effect of etching on bulk mechanical properties was evaluated using an Instron 68TM-30 universal tensile machine. A 5 kN load cell measured compressive force. Tests were performed at a speed of 1 mm/min under room temperature conditions. The specimen dimensions matched those of the substrate used for treatments.

2.5. Culture, buffer media, and epifluorescence stain preparation

A 500 ml of nutrient broth was made using 13 g of broth powder which was dissolved in 500 ml of milliQ DI water. PBS solution was prepared by dissolving 1 × PBS tablet in a 500 ml of milliQ DI water. Both Nutrient broth and PBS solution was sterilised by autoclaving using Tomy autoclave SX700 at 121 C for 20 min. Epifluorescence dye was prepared using LIVE/DEAD™ BacLight™ Bacterial Viability Assay kit (Invitrogen detection technologies, L7012). A 6 μl volume of each dye from SYTO9 and PI was mixed with 988 μl of sterilised PBS in the dark.

2.6. Antibacterial studies

The treated surfaces tested for bacterial attachment using *P. aeruginosa* (ATCC-27853; Gram-negative) bacteria via Live/dead bactericidal viability assay using LIVE/DEAD™ BacLight™ Bacterial Viability Assay kit. Before the assay, samples were fan dehydrated in a dehydration oven at 40 °C for 3 h to remove trapped ethanol and moisture and subsequently sterilised for 20 min under UV light exposure inside the biosafety cabinet. A colony of *P. aeruginosa* bacteria was streaked from sub cultured bacteria plate and incubated in a 5 ml nutrient broth for 16 h using an Eppendorf shaker incubator at 220 rpm and 37 °C. Incubated solution was centrifuged (Beckman Coulter, Allegra X-15R centrifuge) at 5250 rpm for 5 min at 37 °C and decanted the

supernatant to get the pellet. The bacteria pellet was resuspended in PBS and mixed well using a vortex mixer and diluted until obtaining an optical density at 600 nm (OD_{600}) value to ~0.1 [72,79] using the Eppendorf BioPhotometer. Sterile substrates were then added into a 24 well microwell plate and 600 μl of bacterial suspension was added to onto each sample inside the microwell plate. After incubating the bacteria on the PLA samples for 1 hour, the bacterial solution was decanted. Subsequently, the samples were kept at an angle inside the microwell plate for couple of minutes to drain the supernatant liquid. Then transferred into a new microwell plate for further draining before staining. A well cleaned μ-Slide 8 well high glass bottom well plate was used and 2 μl of fluorescence dye (1:1 mix of PI and SYTO9) was added. Wetted samples were drained and placed on the dye solution. After incubating 15 min, samples were imaged using Nikon ECLIPSE TiS inverted fluorescence microscopy via 40X objective lens with FITC and CY3 filters. Capture area was 206.40 μm x 165.12 μm with a resolution of 1280 × 1024 pixels. A control sample (untreated 3D printed PLA), ~100 % live bacteria (test SYTO9), and ~100 % dead bacteria (ethanol added; test PI) were used in this study. Each sample was imaged in 10 distinct locations with 80–120 ms exposure time to evaluate the BE. Images were post processed (color balance, thresholding, and binarization) via Fiji imageJ 1.53t software for counting live/dead bacteria. Moreover, as *P. aeruginosa* is a rod shaped bacteria, it is visible as either a circle (circularity: 0.43–1 [80]) and/or ellipse (circularity: 0.41–0.87 [80]) through fluorescence microscopy when the bacteria oriented in different orientations on the sample. Hence, based on the binarized image, particles above a certain threshold brightness were calculated by assuming the circularity of the bacteria in the range of 0.2–1. The BE of each experiment was calculated via **Equation S2** and **Figure S3**.

2.7. Bacteria fixed SEM

A *P. aeruginosa* bacterial solution with 0.1 (OD_{600}) turbidity was prepared using the procedure described in Section 2.5. Bacterial solution was added to the treated samples (inside a microwell plate) and incubated inside the biosafety cabinet for 1 hour. After incubation, the bacterial solution was decanted from the samples. Next, 600 μl of 2.5 % glutaraldehyde in PBS was added to each sample for bacterial fixation, and the samples were then stored in a biosafety cabinet for 2 h. Following fixation, the glutaraldehyde solution was replaced with PBS to rinse the samples. After the PBS was decanted, a buffer rinse was carried out using 600 μl of sodium cacodylate solution added to each sample. This step was followed by placing the samples in the PELCO BioWave Pro microwave for 1 min to dehydrate. The microwave dehydration with sodium cacodylate was repeated once more. Ethanol dehydration followed, where the sodium cacodylate buffer was sequentially replaced with increasing concentrations of ethanol (30 % to 100 % v/v, in 10 % increments). Each ethanol step was carried out in the microwave for 40 s. For the 90 % and 100 % ethanol steps, the process was repeated. After ethanol dehydration, hexamethyldisilazane (HDMS) was used to dry the samples: two 1-minute microwave cycles with HDMS were performed for each sample. Finally, without decanting the HDMS, the substrates were placed inside the fume hood and left to dry overnight. After dehydration, the samples were gold-coated with a 10 nm layer before SEM imaging.

2.8. Statistical analysis

Statistical analysis was performed to compare the resulsts of Ra, skewness, kurtosis, weight of the samples against each treatments, and BE. ANOVA anaylsis was performed via GraphPad Prism software (version 10.4.1) to evaluate the statistical significance of differences in mean values among the groups. A 95 % confidence interval was applied, with statistical significance set at $P \leq 0.05$. The significance levels were interpreted as: ns (not significant) if $P > 0.05$, * if $P \leq 0.05$, ** if $P \leq 0.01$, *** if $P \leq 0.001$, and **** if $P \leq 0.0001$. All the data were plotted with mean values ± standard deviation.

3. Results and discussion

3.1. Optimizing PLA degradation for etching

The etchant was prepared by degrading PLA in different NaOH concentrations (3 $moldm^{-3}$(M), 4 M, and 5 M). According to Schneidar et al., PLA fully degrades within 48 h in a 4 M NaOH concentration at room temperature [81]. The degradation time can be reduced by increasing the temperature [82–85], increasing alkaline concentration [81,82], and decreasing PLA particle size. Hydrolysis or hydrolytic degradation is one of the key reaction that breaks down the polymer chains of PLA into its monomers [81,82,86–92]. PLA hydrolysis typically occurs in several stages: (1) water diffuses into the PLA, (2) amorphous PLA chains undergo hydrolysis, (3) ester bonds in PLA are cleaved, forming water-soluble compounds, and (4) the crystalline phase of PLA is hydrolysed due to the presence of acidic products and carboxylic acidfunctional groups, which as an autocatalyst [91,92]. As a semi crystalline polymer, PLA contains both amorphous and crystalline regions [93,94]. The hydrolytic chain cleavage mostly occurs in the amorphous region due to its preferential hydrolysis behavior, resulting in an increased polymer crystallinity [95–97].

The hydrothermal approach used a saturated solution of degraded products of PLA to control the etching. Lower OH^- concentration of this saturated solution controls the cleavage of PLA's ester bonds, initiating a low level of alkaline hydrolysis. This leads to a chain scission of PLA and produces lactic acid and sodium lactates as degraded products [74]. Moreover, when the saturated solution reaches super saturation under pressure, it causes PLA degradation products to nucleate on the substrate, thus slowing the etching rate. To identify the optimal concentration for the etchant, we tested 3 M, 4 M, and 5 M NaOH solutions to degrade PLA, using them to etch the surface under same process conditions as depicted in Table 1. Degradation experiments were carried out in triplicate to determine the saturated concentration for each alkaline solution and the corresponding saturation time (**Table S1**). As shown in Fig. 3, the average concentrations of degraded PLA products were calculated using **Equation S1** to be 197.5, 280, and 340 mg/mL for 3 M, 4 M, and 5 M NaOH solutions, respectively. These values were obtained under degradation conditions of 65 °C with magnetic stirring at 200 rpm using PLA granules (< 600 μm).

As per the SEM micrographs depicted in Fig. 3 **(b, c)**, homogeneous nanostructures were evident with a considerable nano-features compared to Fig. 3**(a)**. Despite the nanostructures identified at 5 M alkaline concentrations, high alkaline concentrations tend to degrade PLA via hydrolysis compared to lower alkaline concentrations. Additionally, higher concentrations led to bulk degradation rather than surface degradation. Lower concentrations result in reduced hydrolytic degradation, leading to less etching and consequently limited formation of nanostructured features. Hence, the 4 M concentration was suitable for further study using the proposed low-temperature hydrothermal approach.

3.2. Effect of preheating the hydrothermal vessel prior to reaction

According to Kumara et al. and Schneider et al., 3D printed PLA substrates showed higher etching at elevated temperatures during alkaline etching compared to etching at RT. This resulted in a porous nanostructure, indicating that alkaline hydrolysis is accelerated by temperature [74,81]. Temperature inside the hydrothermal vessel plays a crucial role in the surface modification. Since reactor heating relies on convection within a dehydration oven, it is important to examine the reactor's temperature profile to understand the reaction conditions used for surface modification. As shown in **Table S3**, Scenario I was conducted without preheating the vessel. As depicted in Fig. 4**(b)-Scenario I**, it almost took 2 h to reach 67 °C when the set temperature (Oven PV)

Table 1
Low temperature hydrothermal process pilot trial parameters for choosing an optimal alkaline concentration for treatments. Parameters like set temperature, reaction time, and post etching were selected as per our previous study on alkaline wet etching [74].

NaOH Concentrations ($moldm^{-3}$)	Reaction Set Temperature (°C)	Reaction Time (hours)	Post Etching or Cooling Time (hours)	Ethanol Volume (µl)	Saturation Concentration of PLA (mg/ml)	PLA Solution Preparation Temperature (°C)	PLA Solution Filtration Temperature (°C)	Preheating Vessel Components
3	80	2	22	300	~197.5	65	RT	No
4	80	2	22	300	~280	65	RT	No
5	80	2	22	300	~340	65	RT	No

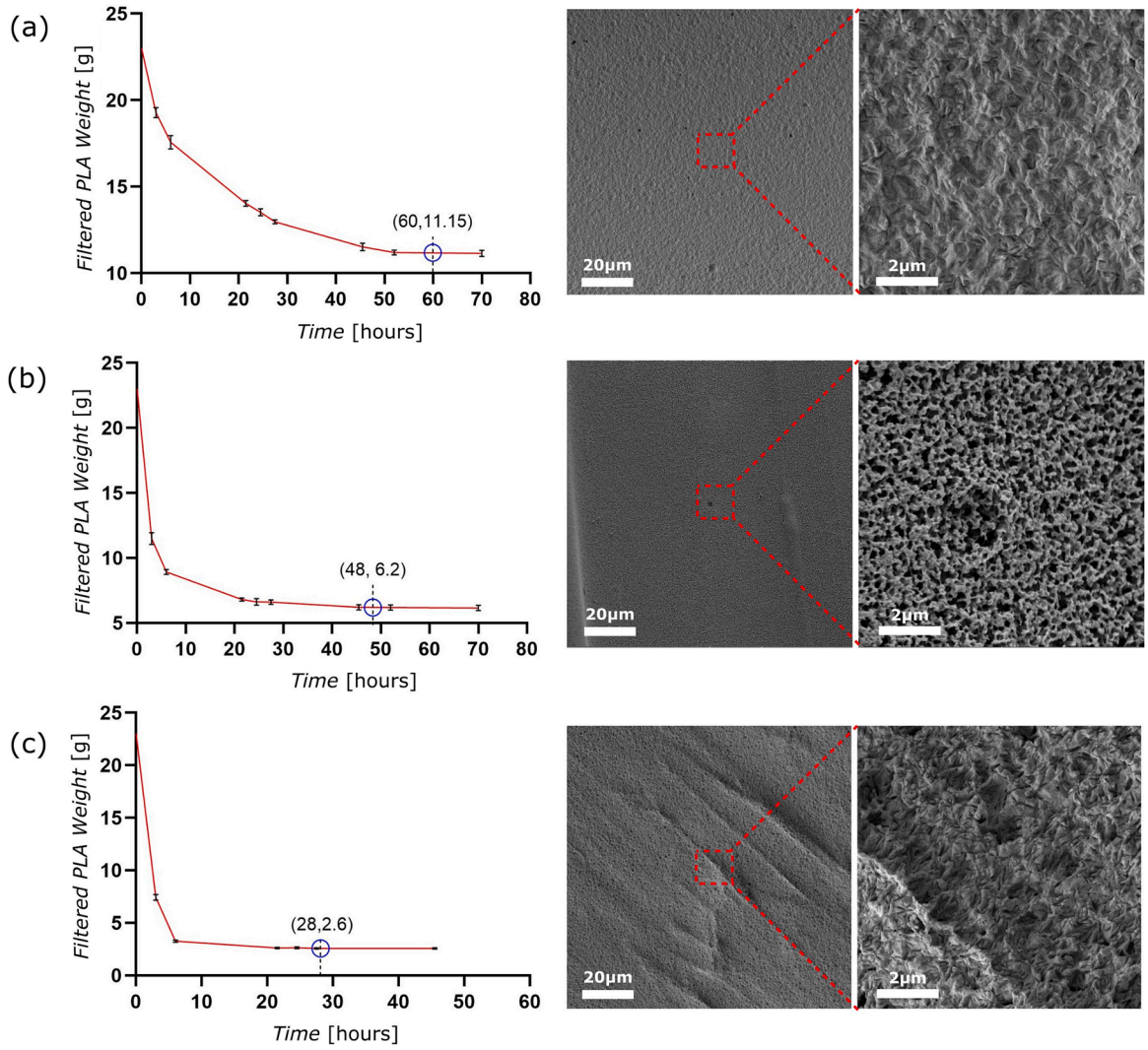

Fig. 3. PLA degradation profiles (average filtered PLA weight Vs time) under 3 M (a), 4 M (b), and 5 M (c) NaOH concentrations. Error bars indicate the standard deviation ($n = 3$). SEM micrographs of treated 3D printed PLA substrates via low-temperature hydrothermal treatments under different alkaline concentrations: 3 M (a), 4 M (b), and 5 M (c). The time required to reach saturation of PLA degradation products at each NaOH concentration is denoted as $t_{x,y}$, where the subscript x represents the NaOH concentration and y denotes the degradation temperature of the solution. Degradation times were 60 h ($t_{3,65}$), 48 h ($t_{4,65}$), and 28 h ($t_{5,65}$). Added PLA granule weight was 23 g in each degradation experiment. Degraded PLA weights were 11.85 g, 16.8 g, and 20.4 g respectively.

was 80 °C. After reaching 70 °C, the temperature plateaued after an additional 3 h. This implied that if the reaction ran for 2 h, the temperature of the liquid inside the Teflon vessel will increase from 20 to 67 °C. However, the participation of thermal energy in the hydrolysis process is limited. This can be compensated by preheating the vessel components before starting the reaction process (**Figure S4**). As shown in Fig. 4**(c)-Scenario II,** preheating will reach thermal equilibrium after 90 min, with the temperature stabilising at 73 °C. This preheating was done without heating the Teflon container, substrates or the solution. Once the vessel components reached equilibrium, the sample holder (Fig. 4**(d)**) and Teflon container (Fig. 4**(e)**) were quickly added into the stainless-steel vessel. For these scenarios, ethanol (99.5 % v/v) was added to increase the partial pressure inside the vessel, thereby promoting oversaturation of the hydrolysed products of PLA.. It was challenging to add ethanol in Scenario II due to the evaporation of ethanol at a higher temperature range (40–73 °C, assembling temperature) unlike Scenario I (RT). A 300 µl of ethanol was injected into the solution using a 1 ml capacity syringe and assembled the vessel parts within few minutes to minimise ethanol evaporation and heat loss to the environment. The solution reached near thermal equilibrium zone after 80 min. During

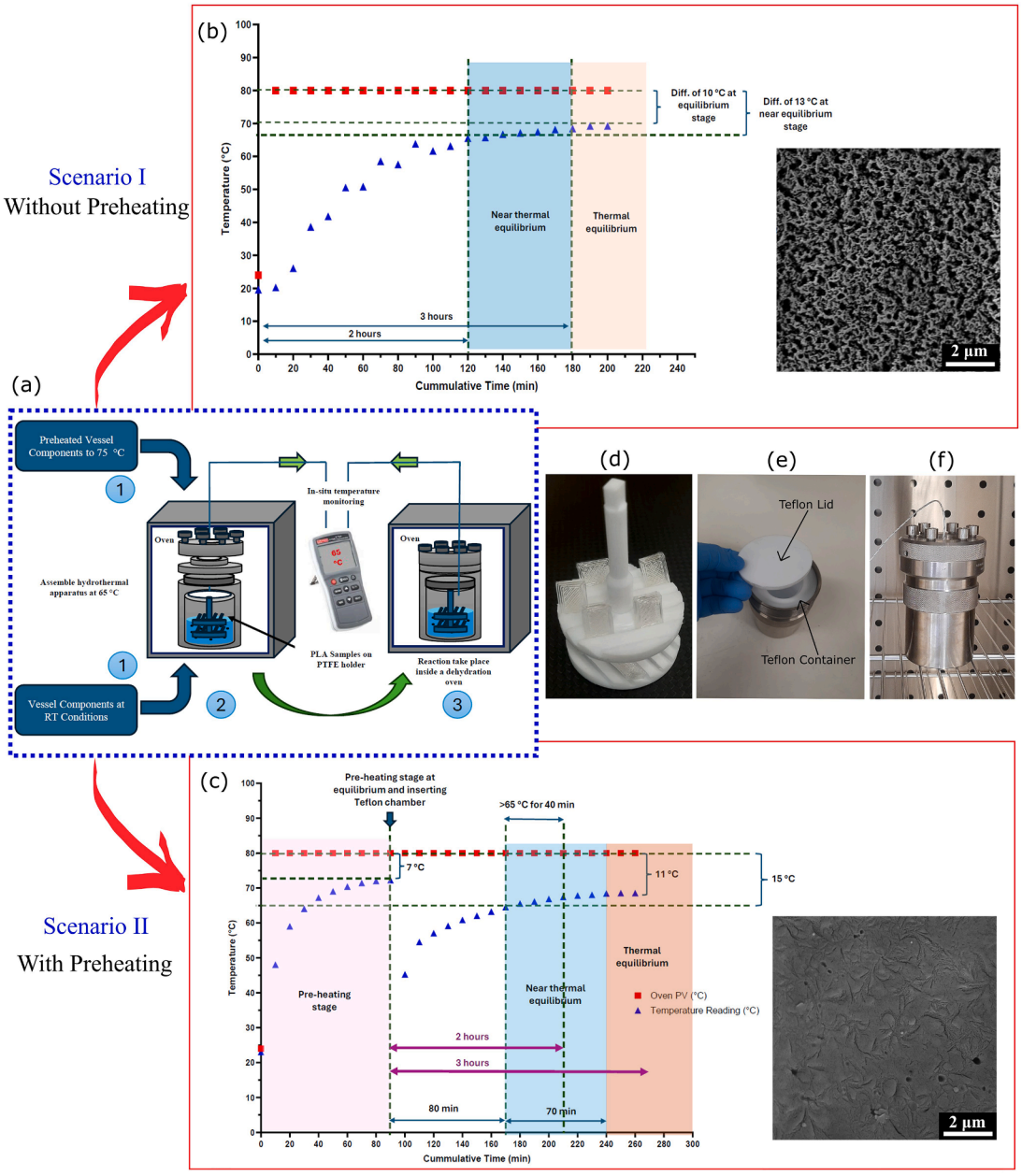

Fig. 4. a) Low-temperature hydrothermal process; Step 1: With or without preheating conditions of the vessel components, Step 2: Assemble hydrothermal vessel, Step 3: Reaction take place inside oven with in-situ temperature monitoring; b) Temperature profiles inside the vessel during the reaction without preheating (starting temperature is RT) condition and corresponding SEM micrograph; c) Temperature profiles inside the vessel during the reaction with preheating (preheating temperature is 75 °C) condition and corresponding SEM micrograph. Set temperature of the oven is at 80 °C for both scenarios. (d) Mounted 3D printed PLA substrates at an angle of 45° on the Teflon sample holder with two decks. (e) Inserted Teflon container inside the stainless-steel hydrothermal vessel and the Teflon sealing lid (f). Assembled hydrothermal vessel equipped with K-type thermal probe placed inside the oven.

this time, the solution temperature increased to 65 °C.

After 2 h, solution temperature reached 68 °C without preheating. However, the solution achieved thermal equilibrium after 150 min, stabilising at 69 °C. Most importantly, in Scenario II, the solution temperature remained above 65 °C for 40 min within the 2-hour reaction time, whereas in Scenario I, the solution temperature was above 65 °C for only 10 min. After the 2-hour low temperature hydrothermal reaction, the vessel was taken out from the oven and kept inside the fume hood for 22 h to cool down to RT in both scenarios. During the cooling process, solubility decreased until the solution reached RT and approached near saturation again. This saturation is further accelerated due to condensation of partially evaporated ethanol due to reduced pressure inside the reactor. Since the main compounds of PLA after alkaline hydrolysis are lactic acid and its salts [74], cooling could lead to the nucleation of these salts.

As per the micrographs shown in Fig. 4 **(b and c),** it is evident that the absence of preheating led to the production of a surface with nano-features, whereas preheating exposed more heat and reduced the tendency to form nano-features. When the temperature exceeds the GTT of PLA, the polymer transitions to a rubbery state, resulting in a smoother surface [98]. This could even tend to warp and change the mechanical properties in large amounts compared with Scenario I. Therefore, for comprehensive surface modification, a preheating condition is not preferred.

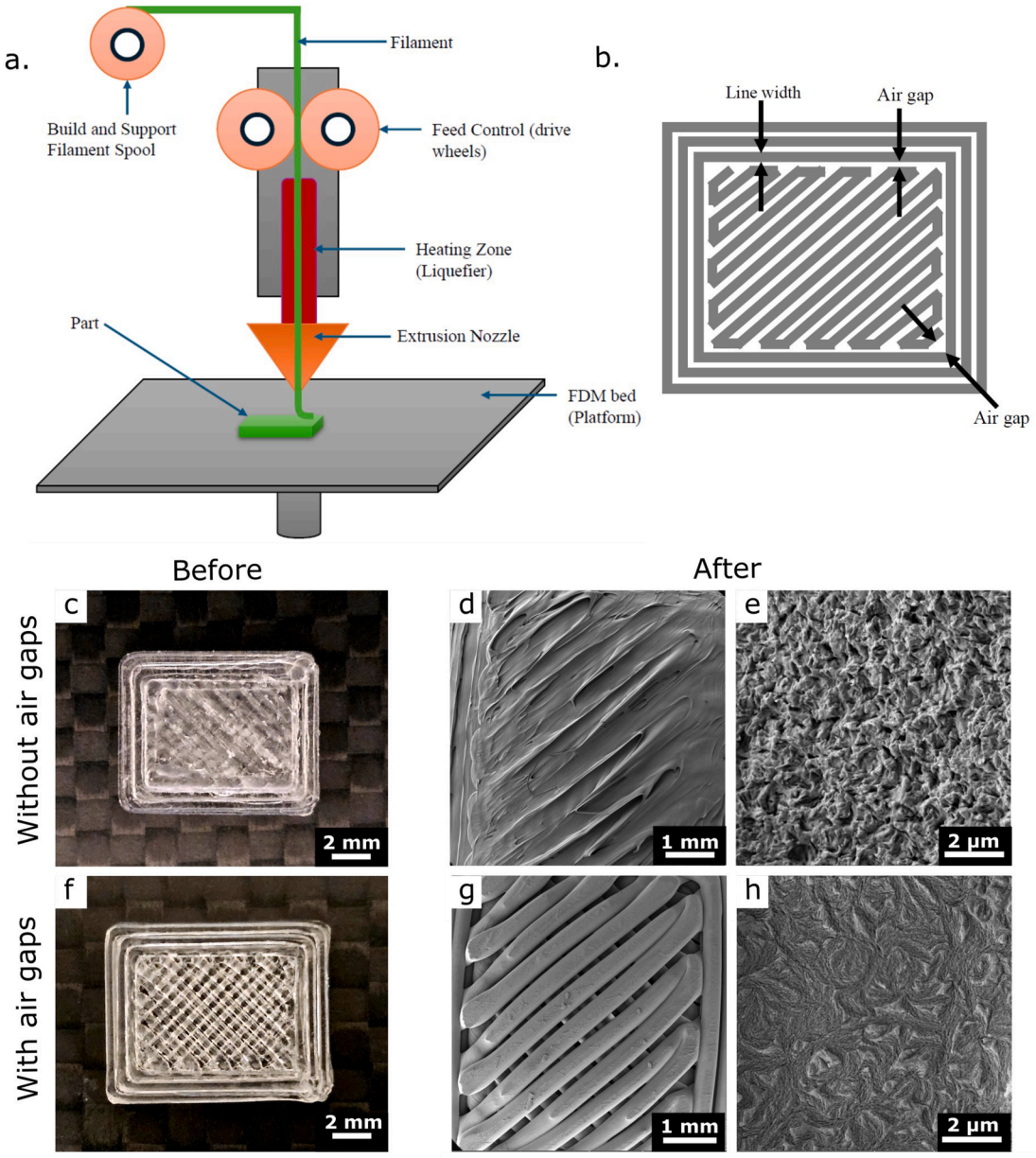

Fig. 5. a) FDM schematic diagram; b) 3D printing nozzle path; c) 3D printed PLA substrate without air gaps (Type 1): This surface was identified as a suboptimal surface for nanostructure modification due to low quality 3D printing; d) Widefield SEM micrograph of treated Type 1 substrate; e) SEM micrograph of treated Type 1 substrate; f) 3D printed PLA substrate with air gaps (Type 2): This surface was identified as an optimal surface for nanostructure modification due to high quality 3D printing; g) Widefield SEM micrograph of treated Type 2 substrate; e) SEM micrograph of treated Type 2 substrate; f) 3D printed PLA substrate with air gaps.

3.3. Effect of 3D printing on surface modification

A FDM 3D printing process was used to print PLA substrates. Two different types of surfaces were obtained: **Type 1** (rough PLA substrates without air gaps) and **Type 2** (PLA substrates with air gaps). Type 1 surfaces were rough due to the bed vibration and dragging the nozzle tip on the substrate when moving to the next position. Additionally, variations in nozzle temperature altered the rheology of the molten PLA [99], causing air gaps to close and the line width to increase, ultimately joining adjacent 3D printing lines together to form a solid substrate without gaps (Fig. 5 (d and e)). Type 2 surfaces, on the other hand exhibited air gaps between the lines, as shown in the nozzle pathway in Fig. 5(b) and widefield SEM micrographs in Fig. 5 (d and g) [100]. Therefore, two distinct substrates were obtained in the same 3D printing batch as depicted in Fig. 5 (c and f). A surface treatment was conducted using the parameters in Table 2 to modify the PLA surface and SEM was used to examine its surface topography to distinguish the effect of the two surface types on the surface modification process. It is clearly visible

Table 2
Low temperature hydrothermal process parameter for identifying the effect of different types of 3D printed substrates in same experiment.

NaOH concentration ($moldm^{-3}$)	Reaction Temperature (°C)	Reaction Time (hours)	Post Cooling and Etching Time (hours)	Ethanol Volume (µl)	PLA Concentration (mg/ml)	PLA Solution Preparation Temperature (°C)
4	90	2	22	300	~280	65

that the nanostructures were able to develop on the 3D printed surface on Type 1 substrate, while Type 2 substrate did not exhibit any nano-features.

The differences in the surface modification observed in Fig. 5 **(e and h)** can be attributed to the variation in surface area between Type 1 and Type 2 substrates. Type 2 substrates had a larger surface area due to the visible air gaps between the line widths, making them more exposed to the etchant. In contrast, Type 1 substrates had a smaller surface area due to the absence of air gaps. Since hydrolysis begins at the surface, the etching depth was greater in Type 1 substrates, which led to etching propagating into the bulk material during the reaction. However, for Type 2 substrates, the higher surface area resulted in surface etching being more dominant than bulk material etching, leading to fewer nano-features, as shown in Fig. 5**(h)**. This also indicates that the surface modification process via the low-temperature hydrothermal method was highly sensitive to the surface area of the substrates. To achieve nano-features in Type 2 substrates similar to those in Type 1, parameters such as reaction temperature, NaOH concentration, and reaction time could be adjusted. FDM is a widely used 3D printing technique because of its ease of use and affordability [101]. However, achieving high-quality surfaces remains challenging due to defects [101,102]. Optimizing printer parameters or utilizing advanced methods, such as stereolithography (SLA), vat photopolymerization, and direct ink writing can enhance surface homogeneity and repeatability [102–104]. Given the advantages of FDM, Type 2 substrates were selected via a visual inspection to avoid using substrates with print defects (e.g. Type 1).

3.4. Effect of reaction parameters on surface modification

The effect of each parameter in the low temperature hydrothermal approach used in this study was analysed through SEM and AFM analysis under different comparison categories as depicted in Table 3. The categories were used to discuss the effect of post etching time, etchant type, addition of ethanol, reaction set temperature, reaction time, amount of ethanol volume added, and two separate nucleation conditions for the development of nano-features. The surface modification process was conducted inside a hydrothermal vessel under different parameter conditions as shown in Table 3. The parameter optimisation and the nanostructure development while introducing various process conditions such as etching time, ethanol addition and precursor change steps were mentioned in the flow chart depicted in Fig. 6. As per the conclusion made in Section 3.1, a 4 M NaOH solution was used as the precursor in different parameter conditions. Subsequently, a saturated solution of hydrolysed PLA was used as the precursor to control the etching and initiate nucleation.

3.4.1. Effect of post etching

Experiment (Exp.) A and B were designed to investigate the effect of hydrolysis at higher alkaline concentrations. Initially, the reaction in Exp. A was carried out for 2 h, followed by an additional 22 h of post-etching in Exp. B inside the fume hood at RT for further alkaline etching. The etching times (2 hour elevated temperature and 22 hour post etching) were selected for initial reaction based on our previous publish research work [74] The significant ($P \leq 0.001$) increase in surface roughness (Ra) by 5–8 times in both experiments compared to the control is shown in Fig. 7 (Control and Exp. A: AFM) and Fig. 8**(a)**. Despite this increase, there was no significant roughness variation within each experiment, although both exhibited substantial ($P \leq 0.0001$) weight loss compared to the control. This result can be attributed to enhanced hydrolytic degradation under elevated OH^- ion concentrations (Fig. 7 **(Exp. A and B)**, Fig. 8**(b)**). AFM images (Fig. 7 (Exp. A and B)) also confirmed that alkaline etching significantly increased surface roughness compared to the control sample. However, extending the post-etching time did not result in a further increase in roughness; instead, it led to a significant ($P \leq 0.0001$) bulk material degradation (Fig. 7 **(Exp. B)**), which would negatively impact the mechanical properties of the substrate. According to Schneider et al., neither bulk degradation nor significant changes in mechanical properties were observed in 3D-printed PLA subjected to alkaline degradation at room temperature [81]. However, under elevated temperature conditions, the accelerated alkaline hydrolysis may lead to increased bulk degradation and a deterioration of the mechanical properties [74]. To mitigate excessive alkaline etching, either the concentration or post-etching time should be reduced. Instead of modifying these parameters, this study utilized a saturated PLA solution as the etchant, which may help lower the effective OH^- ion concentration, thereby controlling the hydrolysis of the PLA part.

3.4.2. Effect of adding PLA solution (etchant type)

The PLA solution was prepared at 65 °C and subsequently filtered at RT. The temperature drop from 65 °C to RT could decrease solubility,

Table 3
Low-temperature hydrothermal experiment parameters for identifying the effect of each critical parameter for surface modification. Repeated rows of same experiment mentioned near the relevant experiment in the table for comparison. One parameter at a time concept was followed for optimisation except the nucleation 1 category.

Comparison Category	Experiment No	NaOH Concentration ($moldm^{-3}$)	Reaction Set Temperature (°C)	Reaction Time (hours)	Post Etching or Cooling Time (hours)	Ethanol Volume (μl)	Saturation Concentration of PLA (mg/ml)	PLA Solution Preparation Temperature (°C)	PLA Solution Filtration Temperature (°C)	Preheating Vessel Components
Post Etching	A	4	80	2	0	0	0	N/A	N/A	No
	B	4	80	2	22	0	0	N/A	N/A	No
Etchant	B	4	80	2	22	0	0	N/A	N/A	No
	C	4	80	2	22	0	280	65	22.5	No
Ethanol	C	4	80	2	22	0	280	65	22.5	No
Addition	D	4	80	2	22	300	280	65	22.5	No
Temperature	D	4	80	2	22	300	280	65	22.5	No
	E	4	90	2	22	300	280	65	22.5	No
Reaction	D	4	80	2	22	300	280	65	22.5	No
Time	F	4	80	2.5	22	300	280	65	22.5	No
	G	4	80	3	22	300	280	65	22.5	No
Ethanol	F	4	80	2.5	22	300	280	65	22.5	No
Volume	H	4	80	2.5	22	600	280	65	22.5	No
Nucleation 1	F	4	80	2.5	22	300	280	65	22.5	No
	I	4	80	2	22	300	280	75	70	Yes
Nucleation 2	H	4	80	2.5	22	600	280	65	22.5	No
	J	4	80	2.5	22	600	280	65	55	Yes

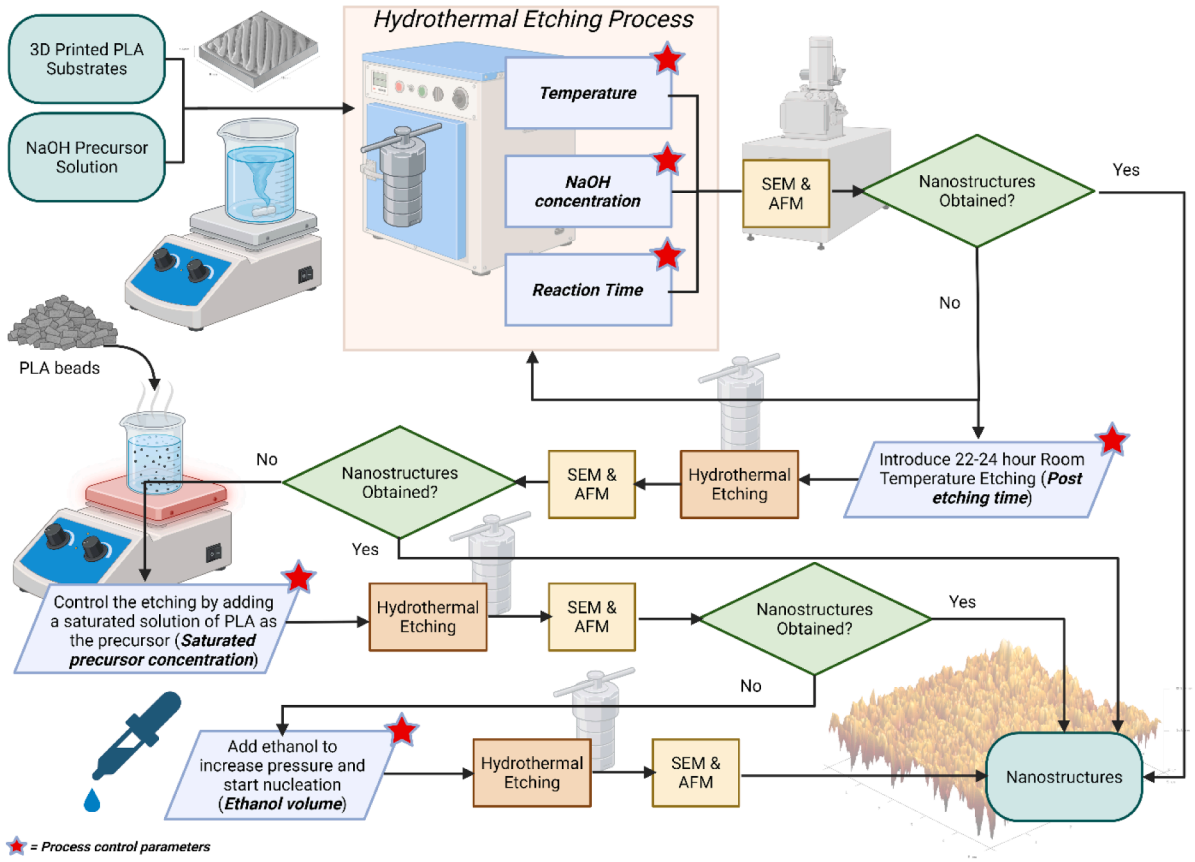

Fig. 6. Low-temperature hydrothermal process parameter optimisation and nanostructure development flow chart Created in BioRender. Sinhasana, B. (2025) https://BioRender.com/tzwbkav.

potentially leading to a supersaturated state and initiating nucleation (**Figure S5**). However, any nucleated material was removed during filtration, resulting in a pale-yellowish solution (**Figure S5**). During the hydrothermal process, the solution temperature increased from RT to 68 °C, as measured using a K-type thermocouple digital thermometer. As the temperature rose from RT to 68 °C, solubility increased, leading to a lower etching rate of the substrates while generating more degraded products through thermo-hydrolysis. The cleavage of PLA's ester bonds via OH^- ions occurred at a lower rate due to the low concentration of free OH^- ions in the solution, as it is close to the saturation state. Furthermore, as the temperature increased from 55 to 68 °C, solubility further increased, accelerating the hydrolysis rate of the samples, particularly as the temperature surpasses PLA's GTT (below 60 °C) [105]. Although SEM images (Fig. 7 **(Exp. B and C)**) showed significant surface modification, AFM images (Fig. 7 **(Exp. B and C)**), Ra values (Fig. 8**(b)**), and kurtosis values (Fig. 8**(b)**) indicated that the PLA solution was able to preserve a surface morphology similar to that observed in Exp. B. Unlike Exp. B, Exp. C did not reduce the sample's weight through hydrolytic degradation. The treated sample maintained its weight under the influence of the PLA precursor solution, rather than experiencing weight loss as observed with NaOH as the precursor (Fig. 8**(b)**).

3.4.3. *Effect of adding ethanol*

The intention of adding ethanol to the solution was to increase the partial pressure inside the vessel to initiate the nucleation and deposit the lactic acid salt on the PLA substrate. This would control the etching while retaining its mechanical strength. According to the SEM and AFM images (Fig. 7 **(Exp. C and D)**) it is evident that the ethanol addition (Exp. D) has made a reduction in spacing in the nanostructures by leaving a high-density nanostructure compared to the sample without ethanol (Exp. C). The total vessel pressure increased to 1.787 bar in Exp. D compared to atmospheric pressure in Exp. C, following the addition of 300 μl. This resulted in the evaporation of 24 % of the added ethanol, as calculated in the supplementary materials (**Equations S3** and **S4** and **Table S5**). The elevated pressure is expected to stabilize saturation or bring the PLA precursor close to saturation. Interestingly, as per the Fig. 8(c), there was no significant ($P > 0.05$) change in roughness or sample weight after adding ethanol. The significant ($P \leq 0.05$) increase in kurtosis value (>3: Leptokurtic) implied that the ethanol addition increased sharp peaks[106] and deep valleys while the decrease in skewness (negative skewness) implied the availability of more valleys with pockets than peaks [107]. SEM images further supported this, showing a more nanoscale pockets than sharp peaks. At 67 °C (equilibrium temperature), with a set temperature of 80 °C, the solution will reach a higher concentration of OH^- ions. This increase was due to the 76 % residual ethanol from the initial addition, which promoted the alcoholysis process [108] and formed pocket like nano-features.

3.4.4. *Effect of temperature*

Temperature is the most crucial parameter in this study since it affects the rate of hydrolysis [74,109]. Increase in temperature will increase the percentage of depolymerisation of PLA via hydrolysis [109]. The increase in temperature from 80 to 90 °C made a substantial effect on the surface modification as depicted in the SEM and AFM images (Fig. 7 **(Exp. D and E)**). Reaction temperatures of 80 and 90 °C were selected to maintain PLA slightly above its GTT but below 100 °C. These conditions minimize substrate warping and enhance both etching and deposition of PLA-degraded products. The deposition is initiated by increasing the partial pressure via ethanol evaporation near its boiling point of 78 °C [110,111]. The measured equilibrium temperature inside the reactor was 76 C. Total pressure inside the reactor was 2.105 bar as per the theoretical calculation (**Table S5**). There was a significant ($P \leq$

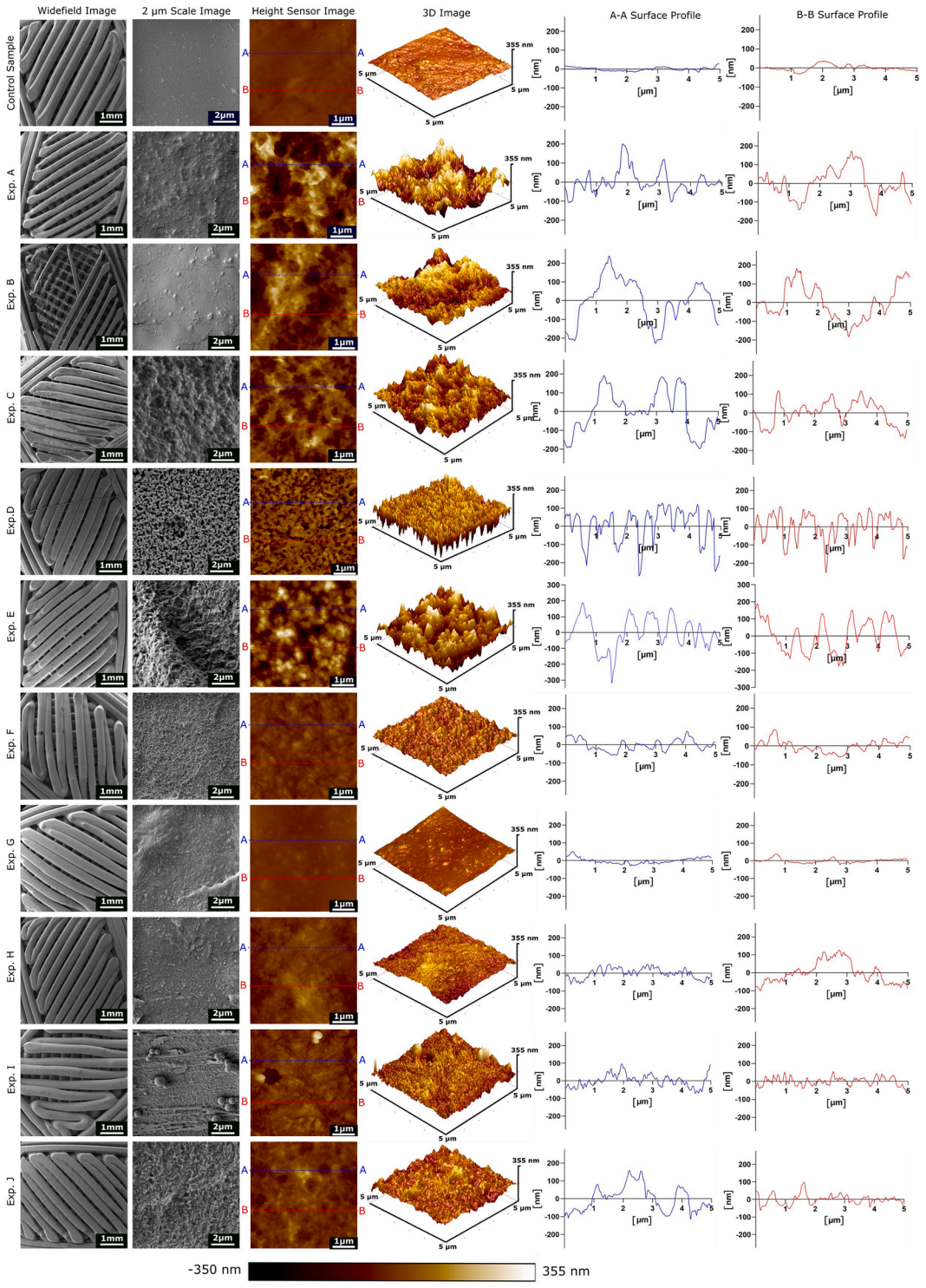

Fig. 7. Widefield (1 mm scale) SEM micrograph, 2 μm scale SEM micrograph, 1 μm scale height sensor image of AFM micrograph, 3D image of AFM micrograph, and surface profiles for A-A and B-B lines of AFM height sensor image are depicted for all the treatments including a control sample (3D printed PLA without treatment). All the AFM images were generated in one scale for comparison as shown in the colour scale bar (max: 355 nm, min: −350 nm). 256 histogram bins, 1st order flattening, 1st order plane fit, and 0.4 aspect ratio were used.

0.0001) improvement in the Ra compared to Exp. D and control sample with this temperature increment (Fig. 8(d)). 66 % of ethanol remained in the solution. Since the equilibrium temperature is close to the evaporation point of ethanol, the total pressure is likely higher than the calculated value. Therefore, increased deposition would be expected. However, no deposition was observed in the SEM images (Fig. 7). This absence may result from the post-reaction cleaning process removing volatile deposited material, or from the solution not having reached equilibrium, leaving the samples subject to etching. The significant ($P \leq 0.05$) increase in skewness (~0) and significant ($P \leq 0.01$) reduction kurtosis (~3: Mesokurtic) of Exp. E compared to Exp. D implied a more distributed nano-features with balanced peaks and valleys [106,107]. There was no significant ($P > 0.05$) change in the weight of the samples compared to control with the temperature increment.

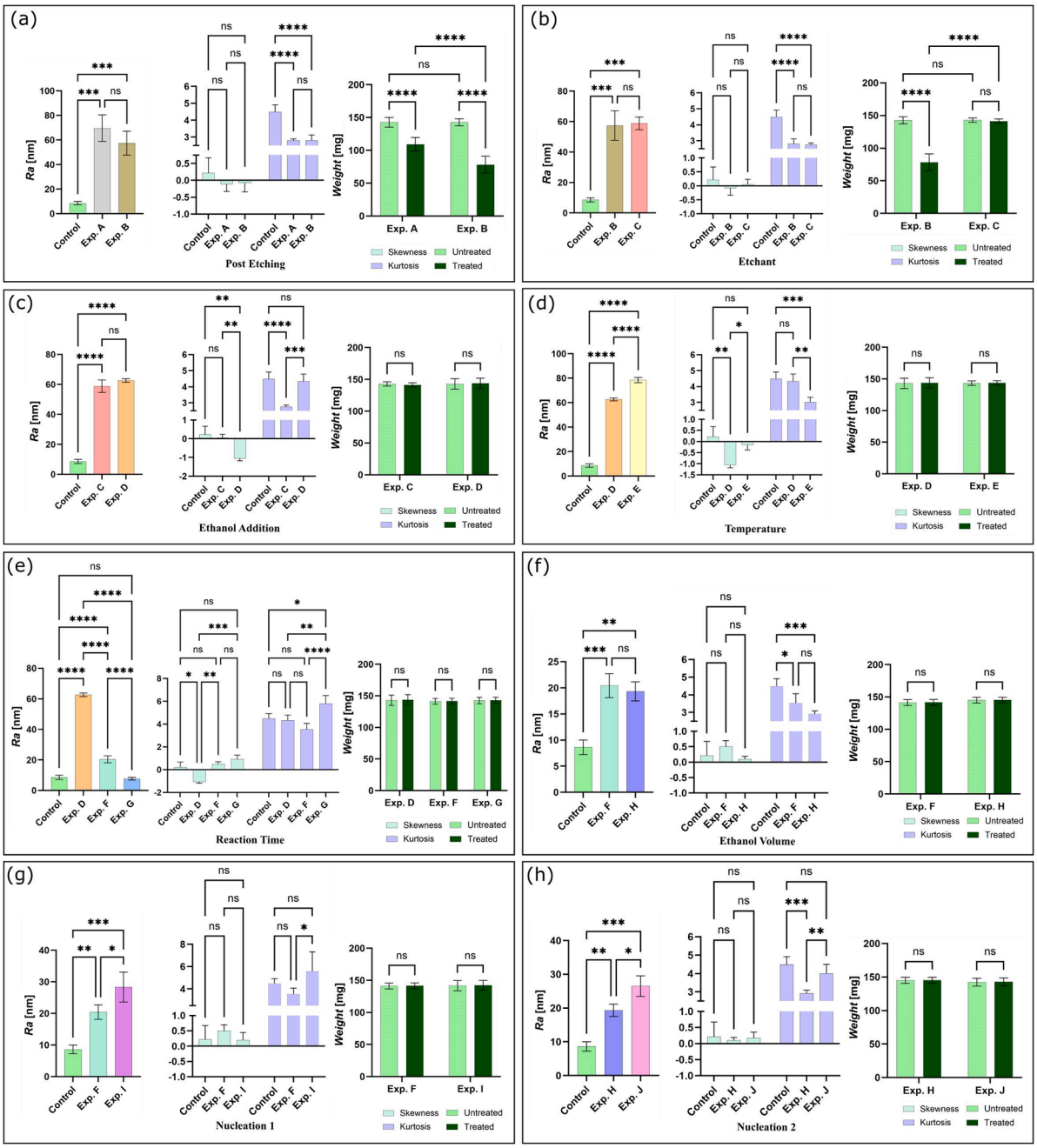

Fig. 8. Statistically analysed results of Ra, skewness and kurtosis, and untreated vs treated weight of 3D printed substrates under different parameter changing conditions such as post etching (a), etchant type (b), ethanol addition (c), temperature (d), reaction time (e), ethanol volume (f), nucleation 1 (g), and nucleation 2 (h). All the graphs show the mean of each data type with standard deviation. $n = 3$ for Ra, Skewness, and Kurtosis. $n = 30$ for sample weight. * shows the ANOVA significance. ns: $P > 0.05$, *: $P \leq 0.05$, **: $P \leq 0.01$, ***: $P \leq 0.001$, and ****: $P \leq 0.0001$.

3.4.5. *Effect of reaction time and ethanol volume*

Reaction time controls the heat exposure and reaction during the treatment. The surface tends to become smoother while reducing the roughness significantly as depicted in Fig. 7 **(Exp. D, F, and G)** and Fig. 8**(e)**. Moreover, the gradual increase in skewness indicated a rise in peaks compared to valleys [107]. Although, there was a significant improvement in kurtosis value (increase in sharp features [106]) at 3 h compared to 2 ($P \leq 0.01$) and 2.5 ($P \leq 0.0001$) hours of reaction, reduction in roughness leads to reduction in nano-features. By comparing the homogeneous surface modification observed SEM and AFM micrographs of Exp. F, the 2.5hr reaction time was optimised with the ethanol volume to increase roughness. However, by increasing the ethanol volume to 300 to 600 μl did not result in any significant change in the surface modification (Ra, skewness, kurtosis, and weight). This conclusion is supported by the total vessel pressure calculations presented in **Table S5**. Although the added ethanol volume increased, the amount of ethanol evaporated remained comparable in Exp. F and H, at 72 μl. Consequently, the total pressure was also similar. Interestingly, as depicted in Fig. 7, the visible nano-features in Exp. F were not observed in Exp. H.

3.4.6. *Effect of nucleation*

The intention of introducing nucleation was to control the deterioration of mechanical properties by controlling the hydrolysis via deposition. Both Exp. F and H studied the nucleation of the saturated PLA solution and deposition during etching and condensation. During the

reaction, ethanol started to evaporate leading to a slight increase in the partial pressure of the Teflon container. A higher total pressure (1.673 bar, **Table S5**) with 600 μl of ethanol and preheating condition led to a decrease in solubility. Hence, there might be a stage that the solution reached its saturation again and started depositing lactide and or oligomers [74,112,113] even without having a catalyst. Moreover, the addition of ethanol in the solution (75 % remained after evaporation at equilibrium) can serve as a dehydrating agent [114,115] during the PLA polycondensation process, helping to shift the reaction equilibrium towards the nucleation. For each nucleation-driven experiment (I and J), the saturated solution was filtered at higher temperatures (55 °C and 70 °C), unlike previous experiments with preheating vessel components, to reduce the heat loss and retain a higher thermal gradient during the reaction. Hence, during the cooling stage, when the temperature decreased below the filtration temperature, the solution became oversaturated and started to nucleate lactide and/or oligomers. There were spherical nanoparticles deposited on the treated surface as depicted in Fig. 7 **(Exp. I)** and Fig. 9**(f).** Given that lactide exhibits a sheet-like morphology with stable crystalline structures [95], the nanoparticles observed may consist of PLA oligomers and/or PLA nanoparticles. These are likely to retain a stable spherical morphology during precipitation [96,116]. Therefore, the process observed in Exp. I appear to resemble a reverse of the hydrolysis reaction. In addition, there was no change in the weight of the treated samples compared to the control. This means that the etched weight was gained through deposition. Even though there was an improvement in Ra compared to control, Exp. F, and Exp. H, there was no significant ($P > 0.05$) change in the skewness and kurtosis values (Fig. 8 **(Exp. G and H)**) compared to the control sample. Deposition of these degraded products from the saturated solution was visible to the naked eye.

3.5. Formation and characterisation of nano-features on hydrothermal etched PLA

Based on the SEM and AFM analyses, Exp. D, E, F, I, and J demonstrated distinct nanostructures as depicted in Fig. 7 and Fig. 10, indicating potential antibacterial activity. Exp. D produced closely packed, pocket-shaped nano-features (Nano-Pockets) with an approximate pore diameter of ~275 nm (**Figure S6**). The formation of Nano-Pockets can be attributed to the addition of ethanol, which accelerates hydrolysis [117], increases the OH^- concentration, and raises the partial pressure, resulting in a higher temperature under the assumption that the vapor above the etchant follows the ideal gas law (see supplementary). Interestingly, weight measurements of the treated samples indicated no bulk degradation, as no change in weight was observed (Fig. 7 (c)). These findings suggest that Nano-Pocket formation occurred preferentially at the surface rather than within the bulk material. Several nanostructures formed via the proposed low-temperature hydrothermal approach resembled morphologies observed in nature. For example, Exp. E generated features resembling the structure of *Sparassis crispa* mushrooms [118]. Hence, they were designated as Nano-Sparassis I, while a similar morphology observed in Exp. J was named Nano-Sparassis II. Due to the highly random distribution of these features, accurately measuring feature spacing or height was challenging. Nonetheless, Nano-Sparassis I exhibited distinct tips with an approximate diameter of 110 nm and an irregular spacing range of 300–1100 nm. Interestingly, Exp. F resulted in fern plant-like nanostructures (Nano-Fern) characterized by very narrow gaps (<50 nm) between individual features. Temperature was the primary parameter influencing the transformation of Nano-Pockets into Nano-Sparassis I and Nano-Fern surfaces, as the temperature increased from 80 to 90 °C and the reaction time extended from 2 to 2.5 h. This transformation is likely due to the polymer being exposed to temperatures above its GTT, which increases chain mobility and induces a rubbery state, resulting in the filling of the pockets. Additionally, Experiment I displayed micro-scale surface

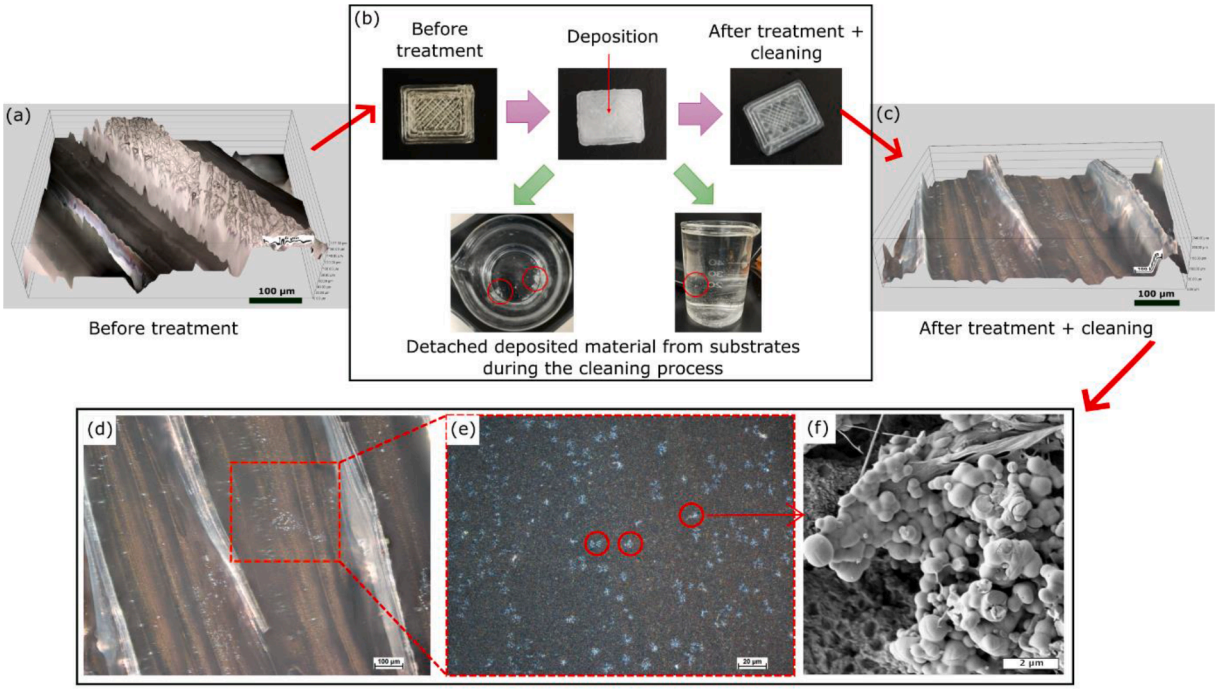

Fig. 9. Nucleation of degraded products of PLA on the substrate during the reaction. a) 3D polarised micrograph of untreated surface; b) Material deposition via low-temperature hydrothermal treatment. The attachment of these degraded products is volatile and some of them were detached from the surface during the sample cleaning process (shown in red circles); c) 3D polarised micrographs of treated cleaned surface. Material deposition was visible even after the thorough cleaning process via 99.5 % v/v ethanol, milliQ DI water, and N_2 gas; d) 2D polarised micrograph of treated cleaned surface; e) Enlarged 2D polarised micrograph of treated cleaned surface; f) SEM micrographs of interested areas (circled in red) shown in the image (e).

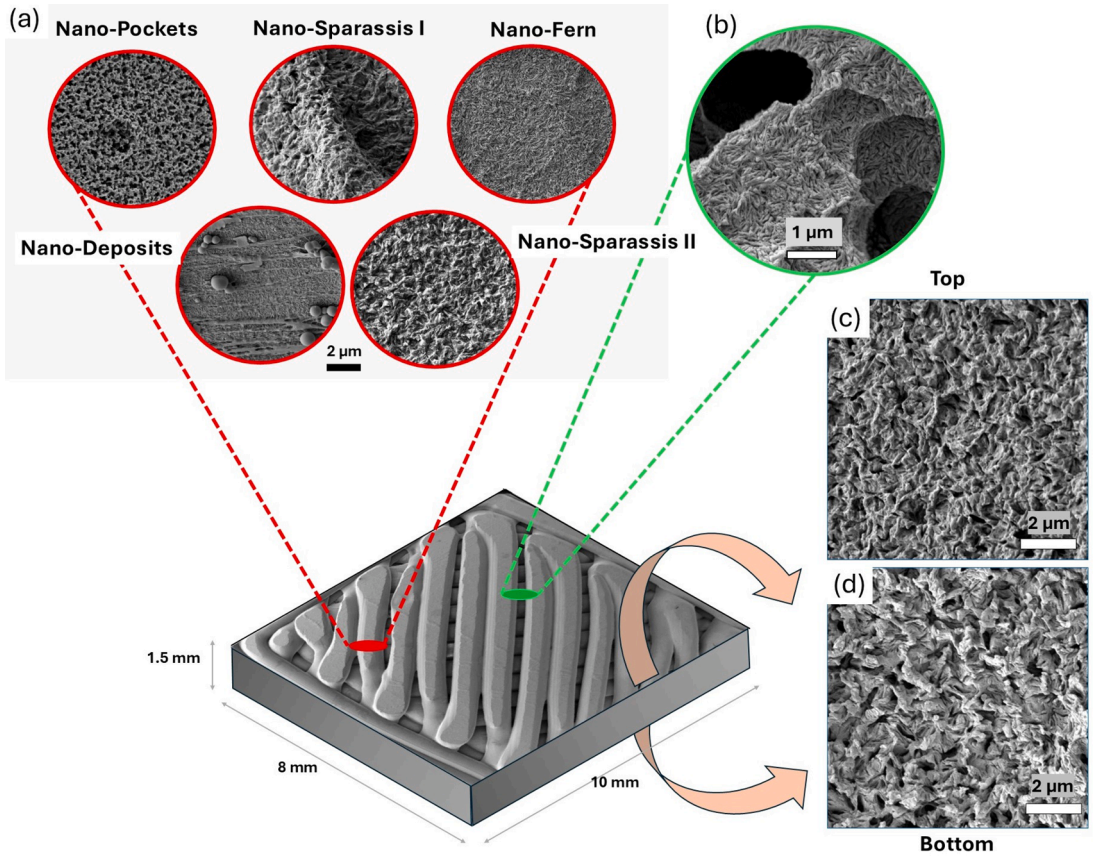

Fig. 10. a) Different nano-features obtained via low-temperature hydrothermal treatment; b) Nano-Fern features inside the microscale pockets; c) Nano-Sparassis I features developed on the top side of the 3D printed sample; d) Nano-Sparassis I features developed on the bottom side (bed side on 3D printer) of the 3D printed sample.

deposition of nanoparticles (100–600 nm in diameter), referred to as Nano-Deposits. Surface deposition was clearly observed as a result of the condensation of saturated PLA degradation products. Whereas these nano-features were fabricated in all the side of the cuboid shape 3D printed substrate as depicted in the Fig. 10 **(c and d)**. Moreover, 3D printed surfaces had micro and macro scale surface deviations including pockets. Nano-features were also seen inside these pockets and micro/macro scale deviated places homogeneously (Fig. 10**(b)**), indicating the possibility of adapting this technique for complex 3D shapes.

3.6. Surface chemistry alterations in PLA via low temperature hydrothermal etching

XPS survey spectrum shown in Fig. 11(a) demonstrated that treated 3D printed PLA substrates consisted of C, O, and Na. In detail, the C, O, and Na peaks corresponded to 298–270, 545–520, and 1075–1070 eV binding energies. Furthermore, it is obvious that the presence of the Na peak only in the treated samples was due to the hydrothermal treatment leaving Na^+ ions to bond with lactate ions producing due to the cleavage of ester bond of PLA. Different compositions of these elements found in XPS spectrum (Fig. 11(b)) attributed to different treatment conditions shown in Table 3. Even though all the samples had gone through a thorough cleaning process, Na was available in different amounts in all the treated surfaces (Atomic weight percentage of Exp. D: 0.65 %, E: 7.25 %, F: 2.29 %, I: 0.62 %, and J: 4.42 %). This was also evident in Fig. 9. To better understand the distribution of Na on the PLA surface, Secondary Electron (SE) and Backscattered Electron (BSE) images were analysed via SEM-Energy Dispersive Spectroscopy (EDS). The EDS images shown in Fig. 11 (d and e) demonstrated a clear difference between SE and BSE images, which could be attributed to spread sodium lactate on the surface. To get more information about the composition variation on different locations (location 1, 2, 3, and 4 shown in Fig. 11(e)), EDS point analysis was performed. Analysis confirmed that all the locations had Na as an element and the concentration was high in location 1 and 3 (Fig. 10**(e)**). See **Figure S7** for more EDS elemental analysis. This was also evident in high contrast of these locations in BSE image. To conclude, irrespective of the location, most treated sample areas contained Na. The Au peak identified in the EDS spectrum shown in Fig. 11 (f-i) was due to the Au coating on the sample for SEM imaging. This coating makes the polymer samples conductive and ideal for SEM imaging, as it helps limit sample drifting and charging.

The broad peak (L), which was identified in the FTIR spectrum (3125–3750 cm^{-1}) in Fig. 11(c), was related to the presence of an O—H functional group [74,75]. This peak was not identified in the control and Exp D (Nano-Pockets) and E (Nano-Sparassis I), however, a broad peak was identified in Exp. I (Nano-Deposits). The presence of this peak at low amplitudes in other samples can be attributed to OH^- ions from the hydrolysis process and remaining ethanol due to the cleaning step. Notably, the Nano-Deposits sample, which exhibited a more prominent OH^- ion peak, demonstrated the lowest BE among the treatments. Therefore, it can be concluded that the ethanol cleaning step has no effect on BE, since any remaining ethanol is eliminated during the dehydration step. The differences or absence of this peak in other experiments could be due to the uneven dehydration process, where moisture and ethanol are removed from the samples. Identical low intensity narrow peaks (M) in the region of 2850–3050 cm^{-1}, could be due to C—H stretching spectrum in the CH_3 functional group [119]. Since this peak was absent in the control sample, its presence in the treated samples may indicate a change of bond angle and length during the reaction. The most dominant high intense peak in these spectrums is

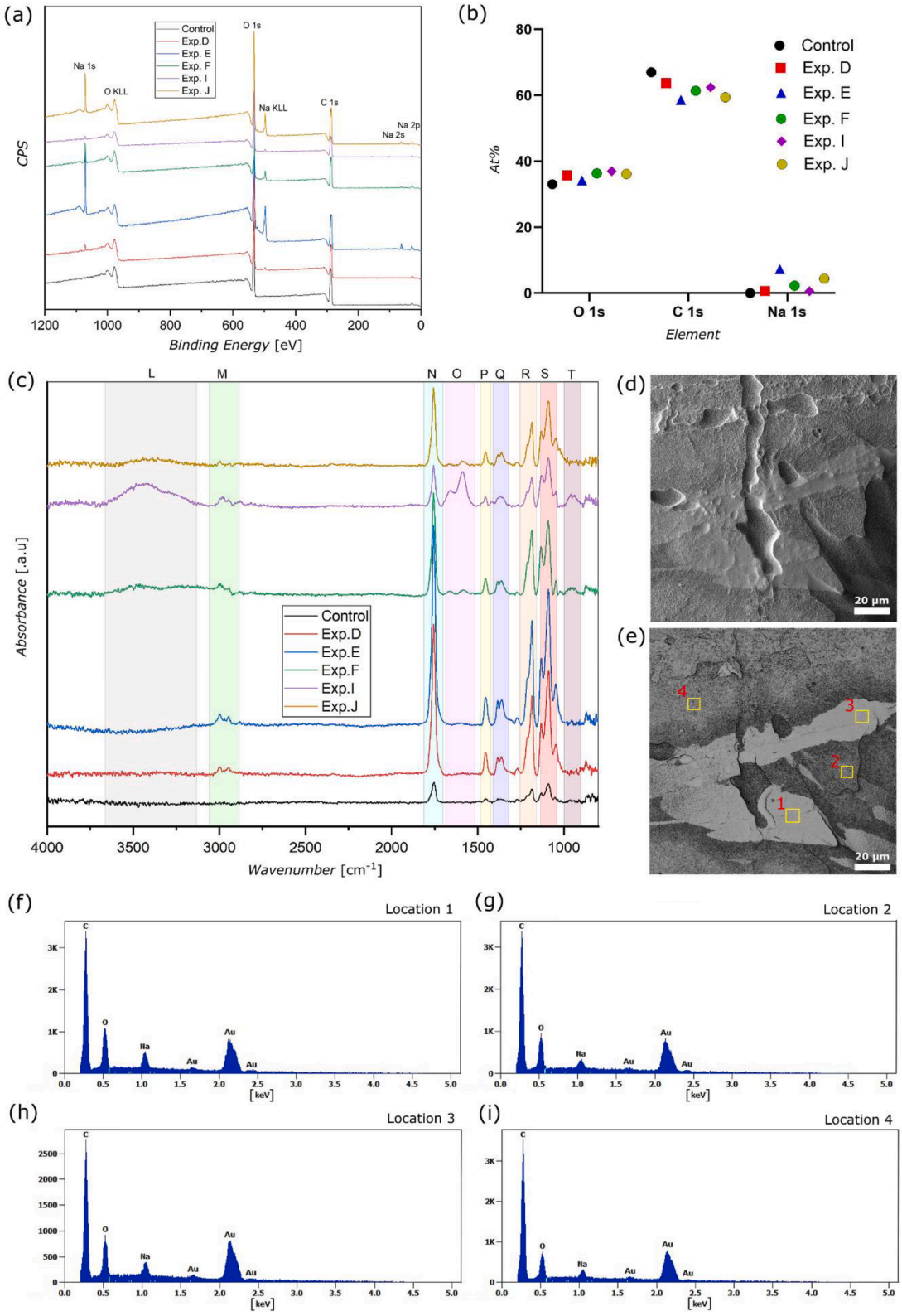

Fig. 11. Surface chemistry analysis of treated surfaces. a) XPS survey spectra; b) Atomic weight percentage of each element found in XPS spectra; c) FTIR spectrums for control and treated samples; d) SE SEM micrograph of treated PLA substrate via Exp. J; e) BSE SEM micrograph of treated PLA substrate via Exp. J. Four locations were analysed to get more understanding about the elemental composition of the surface. Location 1 and 3 were on high contrast locations. Location 2 and 4 were on low contrast locations. f-i) EDS elemental composition peaks relevant to Location 1, 2, 3, and 4.

peak "N", which was identified in the region between 1700–1800 cm^{-1}. This could be due to the stretching vibrations of the C=O functional group from the carboxylic acid carbonyl group of PLA [120,121]. There were no peaks found in between 1500–1700 cm^{-1} in the control sample and Exp. D and E. Interestingly, a high intense peak appeared in Exp. I. This peak is most likely due to a strong asymmetric stretching vibration of the carboxylate group ($–COO^-$), which is due to a high thermal gradient and material deposition compared to other experiments leaving more carboxylate groups. The other intense peaks, which appeared in the region of 1300–1500 cm^{-1} (P and Q) compared to control sample, was due to increased bending vibrations of CH_3, C—H and O—H groups under hydrolysis [74,75,119]. Increased intensity peaks found in the R, S, and T regions in all treated samples could be due to the C—O stretching because of cleaving ester bonds during alkaline hydrolysis. In other words, this implies the increase of C—O functional bond due to producing both lactic acid and lactate salt [74]. To conclude, all the low-temperature hydrothermal treatments resulted in a similar change in the chemical bonds in different intensities except Exp. I. This could be attributed to the more dominant nucleation observed in Exp. I compared to the other experiments. Considering all the XPS, EDS, and FTIR data, we can conclude that the treated sample surfaces contained Na, likely in the form of lactate ($C_3H_5NaO_3$).

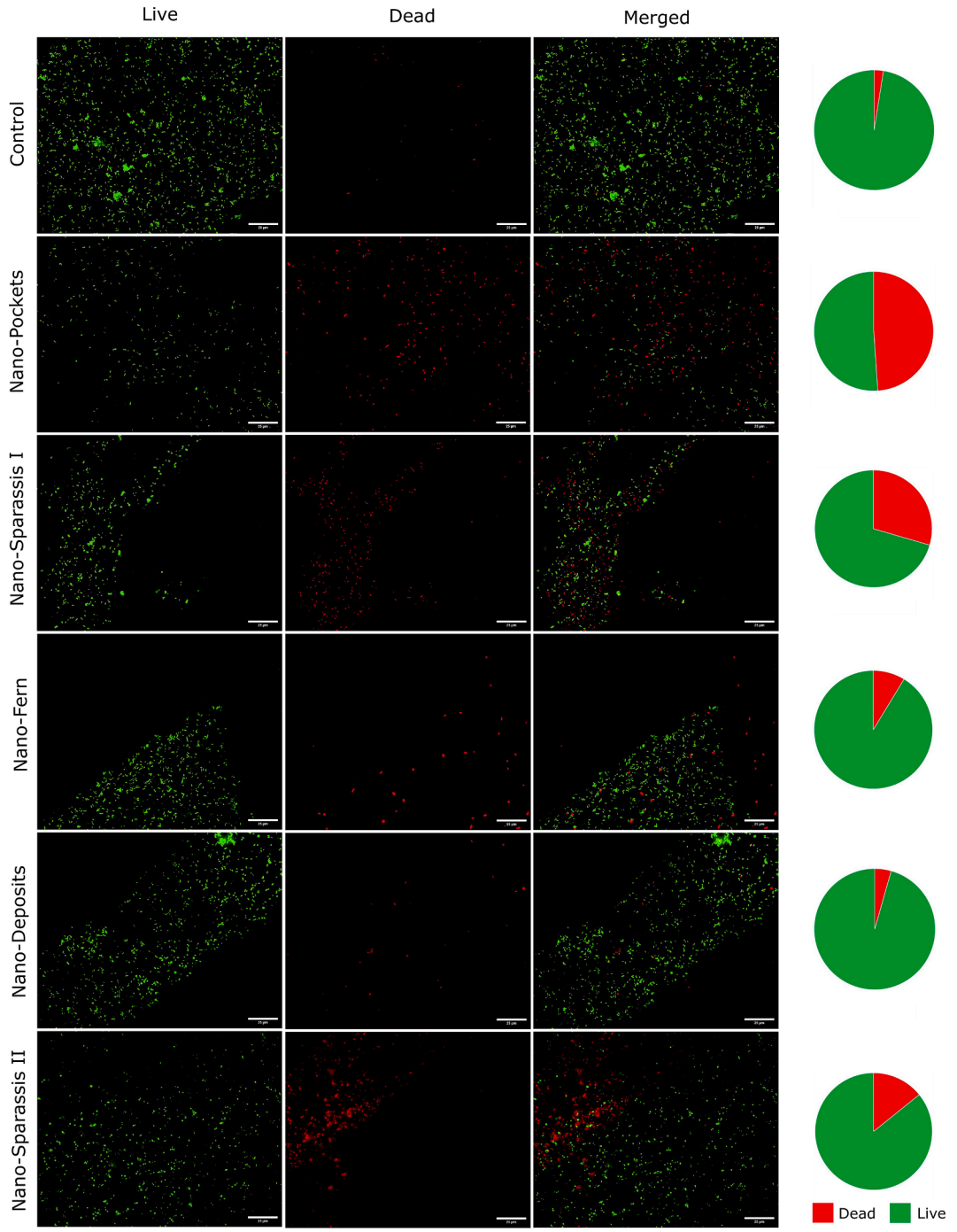

Fig. 12. Live/Dead fluorescence images of bacterial cells on control and treated surfaces. Red colour represents dead cells, and green colour represents live cells in the images. The pie charts shown in each image row represents the corresponding BE % of each surface. Bacterial cell incubated samples were stained with a mixture of Propidium Iodide (PI; red) and SYTO9 (green). Stained samples were imaged via fluorescence microscopy using FITC and CY3 filters. Scale bar: 25 μm.

3.7. Antibacterial activity of hydrothermally etched 3D printed PLA

The BE of 3D printed PLA surfaces of before and after treatments via low temperature hydrothermal approach was tested against *P. aeruginosa* bacteria. Although minimum incubation times of 0.5–3 h have been reported in the literature for various polymeric nano-structured surfaces [39,122–127], an incubation time of 1 h was employed in this study to quantify the maximum BE achievable within a shorter duration. The results showed that Nano-Pockets and Nano-Sparassis I surfaces had a significant ($P \leq 0.0001$) BE (mean values are 48.8 % and 29.5 % respectively) within 1 h of incubation of OD_{600}=0.1 inoculum, while other modified surfaces such as Nano-Fern and Nano-Deposits had comparable (not significant: $P > 0.05$) BE compared to the control sample (untreated 3D printed PLA) as depicted in Fig. 12 and Fig. 13. Interestingly, there were another significant ($P \leq 0.001$) enhancement of BE (14.2 %) in Nano-Sparassis II surface. It is evident that there is no support from the deposited material to the antibacterial activity due to comparable BE % found in Nano-Deposits compared to control surface (Fig. 12). However, It was evident from the SEM and AFM micrographs that Nano-Pockets and Nano-Sparassis to be antibacterial via mechano-bactericidal activity to a certain extent due to its nano-feature arrangement (spacing and height) as per the literature data [2].As shown in the bacteria-fixed SEM micrographs in Fig. 13 (d, e), it is evident that the bacterial cell membranes, indicated by yellow arrows, were structurally deformed or stressed compared to the control substrate (Fig. 13(c)). Some of the bacterial cell membranes were shown

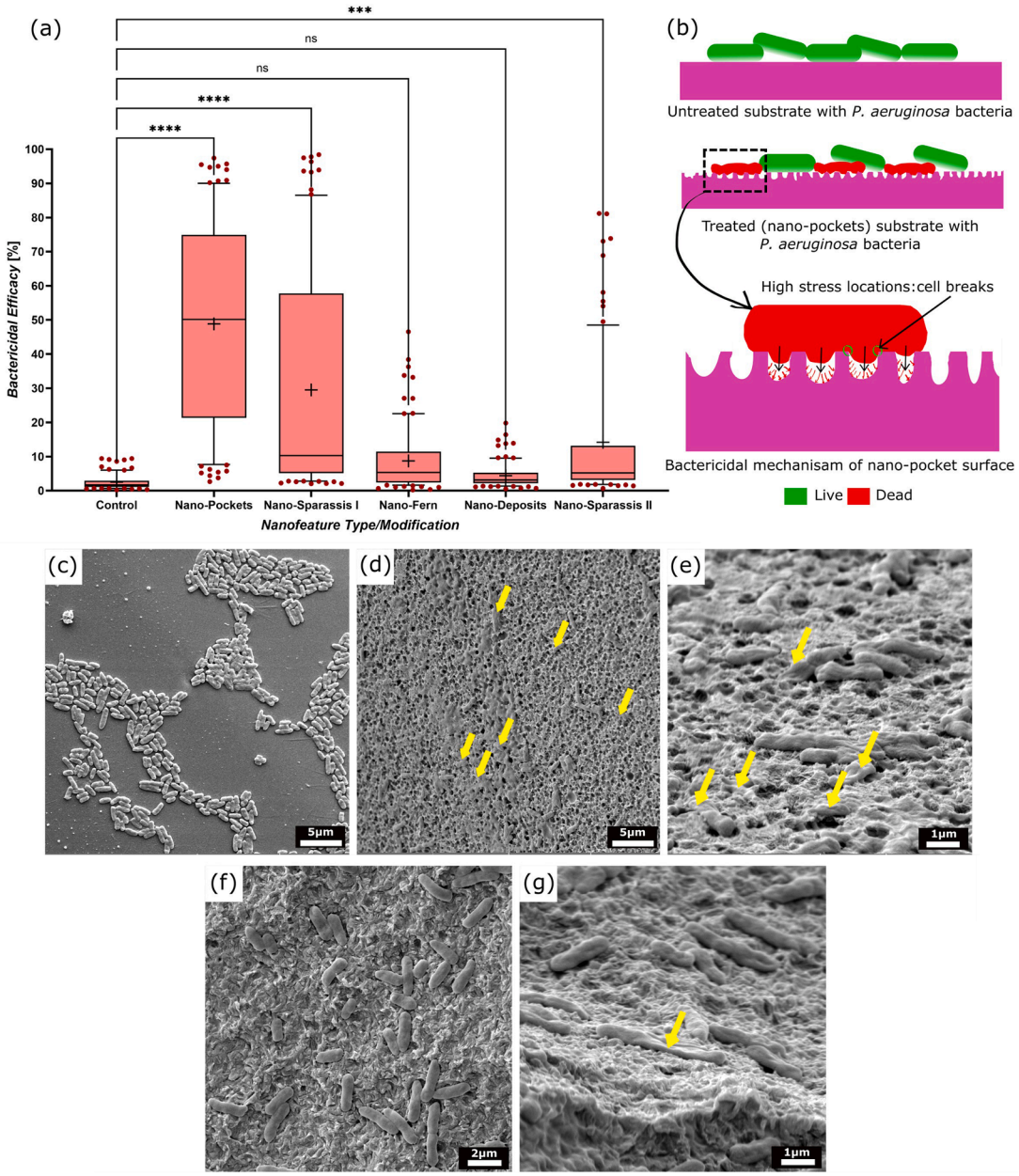

Fig. 13. a) Box plot depicted with median center line with 10–90 percentile points shown with lower and upper quartiles while whiskers extends to the 10th and 90th percentiles. + symbol reperesents the mean BE % of each surface. $n = 90$ data were gathered for each surface (3 replicates, 3 repeats, and 10 images for each substrate). * Shows the ANOVA significance. ns: $P > 0.05$, ***: $P \leq 0.001$, and ****: $P \leq 0.0001$; b) Bactericidal mechanism for Nano-Pockets; c-g) SEM micrographs of P. aeruginosa bacteria fixed on untreated and treated 3D printed PLA substrates: (c) control substrate (untreated), (d, e) bacteria on Nano-Pocket surface via horizontal and 45° angle SEM, and (f, g) bacteria on Nano-Sparassis I surface via horizontal and 45° angle SEM. Stressed/lysed bacteria were shown in yellow color arrows in all SEM micrographs.

high level of membrane damage and oxidative stress due to the prolonged stress produced by the Nano-Pockets [128–130]. The mechanism of this lysing procedure is mechano-bactericidal activity. This occurs when bacteria are attracted more toward the pocket, due to Van der Waals forces, hydrostatic forces, and hydrophilic interactions at the pocket surface [2,129,130]. The bacteria act as a simply supported beam, as shown in Fig. 13(b). As a result, the stress on the support points of the rod-shaped bacteria increases, causing the cell membrane to be stressed and lyse [129,130]. In contrast, only a minimal number of bacterial cells were compromised on the Nano-Sparassis I surface, as shown in Fig. 13**(g)**. Bacteria adhered to the Nano-Sparassis I surface was seen limited cell damaging, as shown in Fig. 13(f). This is because the height and depth of the features on Nano-Sparassis I surfaces are visibly less than those on Nano-Pockets, so they do not produce considerable stress on the cell membrane [131].

Interestingly, 50 % of the Live/Dead data ($n = 45$) was in between 22–72 % and 10 % from these data ($n = 9$) were above 90 % BE (**Figure S8, Table S4**), meaning that there is very significant improvement in BE in Nano-Pockets against *P. aeruginosa* bacteria, but the inconsistency (**Figure S9**) in the surface development caused a higher standard deviation within the results. This is also indicated by having <10 % BE for 10 % surfaces ($n = 9$ for each type of modification) of all the treatments including control. The BE results obtained on 3D-printed PLA surfaces using the novel approach introduced in this study were lower than those on 3D metallic surfaces, which had around 90 % efficiency [58]. This lower efficiency is attributed to the high standard deviation observed in the BE results. To provide context, Jagessar et al. studied the BE of random nanostructures produced via hydrothermal synthesis on 2D and 3D titanium surfaces. Their findings showed that 3D surfaces had a 91 % increase (from 15 % to 25 % approximately) in BE compared to 2D surfaces when tested against Gram-positive *Staphylococcus aureus* [60]. Given that Gram-positive bacteria have a thicker cell membrane than Gram-negative strains, it is expected that these 3D metallic surfaces should demonstrate a higher BE of around 90 % for Gram-negative strains as well [2]. However, there is insufficient literature to compare these findings one to one with those for nanostructured polymeric 3D-printed surfaces.

3.8. Surface modification effect on bulk mechanical properties

Compression failure was evaluated for all treated substrates, as shown in Fig. 14 (b, c). Statistical analysis of the compression test results (Fig. 14(f)) indicated no significant change in the Young's modulus of PLA, suggesting that the overall bulk stiffness were retained after treatment [132]. Since the hydrolytic degradation predominantly occurred in the amorphous regions of the semi-crystalline polymers like PLA, the treated samples exhibited increased crystallinity, which contributed to the retention of stiffness [92,133]. PLA exhibited a compression failure force of approximately 5 kN, with one out of three samples failing at around 4.8 kN. Notably, none of the Nano-Pocket

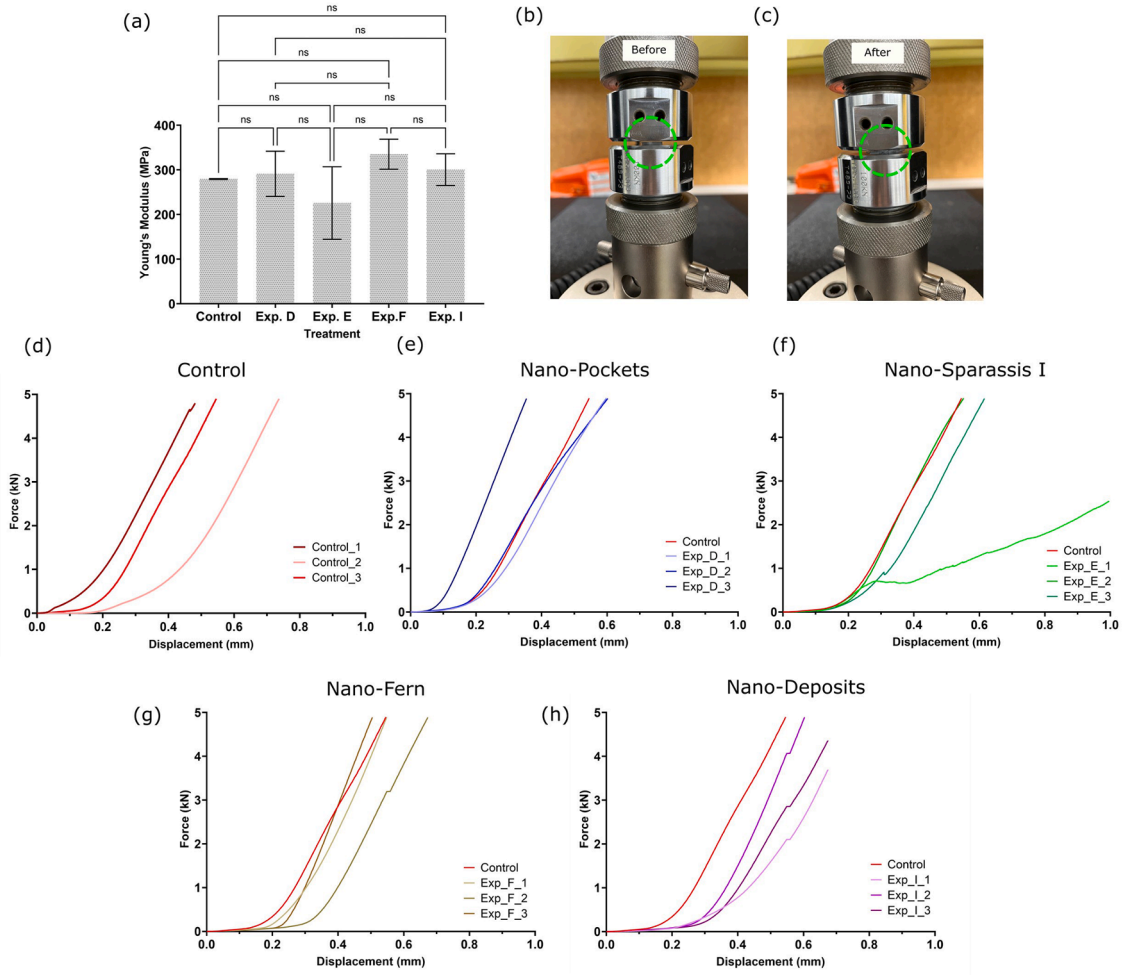

Fig. 14. a) Deviation in Young's modulus of treated substrates during compression tests; b, c) Substrate positioned between compression dies before and after testing. d-h) Force vs displacement plots for the substrates: Control (d), Exp D (e), Exp E (f), Exp F (g), and Exp I (h). Each test was performed in triplicate. Control_3 plot was used to compare the compression behaviour of treated substrates with the control. $n = 3$ data were gathered for each sample (triplicate). * Shows the ANOVA significance. ns: $P > 0.05$.

samples failed under compression, as shown in Fig. 14(e). This result is notable, as Nano-Pocket surfaces demonstrated the highest BE among all treatments. In contrast, two out of three Nano-Sparassis I substrates failed under compression at forces below 1 kN, one Nano-Fern sample failed at approximately 3 kN, and all Nano-Deposits samples failed within the range of 2–4 kN. Although Nano-Deposits were expected to exhibit the highest mechanical properties, they failed under compression more readily than Nano-Pockets. The observed failures in both Nano-Sparassis I and Nano-Deposits are attributed to exposure to high thermal gradients during processing. The set temperature for the Nano-Sparassis I surface was 90 °C, whereas all other treatments were set at 80 °C. Additionally, the PLA solution for Nano-Deposits was filtered at 70 °C during precursor preparation with preheating conditions (scenario II), while filtration for other treatments occurred at RT. These conditions resulted in prolonged exposure to higher thermal gradients for these samples, as shown in Fig. 4**(c)**.

4. Conclusions

In this study, 3D printed PLA susbtrates were successfully modified using a low-temperature hydrothermal approach. A few types of nano-features were developed, which were bactericidal against *P. aeruginosa* bacteria with a maximum BE of 98.4 % within a shorter incubation time (1 h). However, the average maximum BE was 48.8 % (Nano-Pockets). The next highest BE was observed on the Nano-Sparassis I surface with a BE of 29.5 %. The high standard deviation of BE values is attributed to the uneven fabrication (non-homogenous) of nano-features and the randomness (inconsistent spacing, height, and pore diameters) of the nano-features (See **Figure S9**). This is due to the inconsistency in 3D printing due to FDM deffects, which results in substrates with varying surface areas as discussed in Section 3.3. Consequently, this led to inconsistencies in nanostructure fabrication. Despite the FDM's popularity for cost-efficient 3D printing, optimizing its parameters to prevent defects or adopting higher-quality techniques such as SLA, vat photopolymerization, and direct ink writing would better prevent the impact of printing defects on nanostructure formation. In this study, the effect of printing defects was minimized by selecting high-quality prints (Type 2) through visual inspection. Further investigation is warranted to fully understand the influence of printing methods on nanostructure formation. Although the modification process degraded PLA to a certain extent during etching, using a saturated solution of the same material (PLA) helped to control the degradation and retain the overall weight of the substrate. This approach helped in controling the reduction of mechanical properties of the samples. Compression tests and sample weight measurements demonstrated that the bulk mechanical properties were retained to a significant degree. This retention is advantageous for applications such as biomedical implant fixation devices, which are typically subjected to compressive forces and require high stiffness. Interestingly, the lowest mean BE was seen in the Nano-Deposits among all the treatments, despite having highest levels of deposition in the form of PLA nanoparticles, PLA oligomers, and sodium lactate. A low BE of Nano-Deposits indicates that there is no contribution from these chemicals towards the antibacterial activity. Moreover, the FTIR spectrum where the OH^- ion broad peak was absent in Nano-Pockets and Nano-Sparassis showing a comparble peak to the untreated susbtrate. This suggests that the ethanol cleaning step or remaining ethanol on the sample did not influence the antibacterial activity. The higher BE observed for Nano-Pockets and Nano-Sparassis surfaces was due to mechanical lysing via stress producing from nano-feature result in oxidative stress. In other words, rod-shaped *P. aeruginosa* bacteria are attracted to the pockets due to surface attraction forces and rupture of the bacterial cell membrane from the contact points of the bacteria on the circumferance of the near circular shape pockets. These nano-features would provide an ideal environment for the proliferation of human osteoblast cells as per the litrerature studies, which is benificial to maintain cytocompatibility in most of the biomedical applications. Interestingly, this low-temperature hydrothermal approach resulted in the fabrication of comparable nano-features on all sides of the cuboid-shaped PLA substrate. This method lays the foundation for producing nanostructres on 3D printed polymeric surfaces and following further modifications and optimisations will enable paths to use this method for fabricating nanostructures on 3D polymeric surfaces with complex geometries, including internal and external surfaces, specially biodegradable patient specific implants and biomedical equipment.. Looking ahead, these nanostructures are expected to offer valuable solutions accross diverse industrial and biomedical applications.

Funding

This research was funded by "Australian Research Council (ARC) Industrial Transformation and Training Centre for Multiscale 3D Imaging (ARC ITTC M3D) Stryker Scholarship [Project IC 180100008] and Queensland University of Technology (QUT)".

CRediT authorship contribution statement

S.P.S.N.Buddhika Sampath Kumara: Writing – review & editing, Writing – original draft, Visualization, Methodology, Investigation, Data curation, Conceptualization. **Preetha Ebenezer:** Visualization, Data curation. **S.W.M.Amal Ishantha Senevirathne:** Writing – review & editing, Supervision, Methodology, Investigation, Data curation, Conceptualization. **Mohammad Mirkhalaf:** Writing – review & editing, Supervision, Methodology, Investigation, Data curation, Conceptualization. **Prasad K.D.V. Yarlagadda:** Writing – review & editing, Supervision, Methodology, Investigation, Funding acquisition, Data curation, Conceptualization. **Laura J. Bray:** Writing – review & editing, Supervision, Methodology, Investigation, Data curation, Conceptualization. **Asha Mathew:** Writing – review & editing, Supervision, Methodology, Investigation, Formal analysis, Data curation, Conceptualization.

Declaration of competing interest

The authors declare that they have no known competing financial interests or personal relationships that could have appeared to influence the work reported in this paper.

Acknowledgement

Authors acknowledges funding source for the research received from "Australian Research Council (ARC) Industrial Transformation and Training Centre for Multiscale 3D Imaging (ARC ITTC M3D) Stryker Scholarship (Project IC 180100008) and Queensland University of Technology (QUT)". A. Mathew acknowledges the support from VC postdoctoral fellowship for women in STEMM (UniSQ). L.J. Bray acknowledges support from the ARC in the form of a Future Fellowship (FT210100579). M. Mirkhalaf acknowledges the Australian Research Council (ARC) Early Career Award (DE210100975). The authors acknowledge continued support from the Queensland University of Technology (QUT), Dr. Jayanti Mendhi for supporting SEM imaging, Dr. Yanan Xu for supporting AFM characterisations, and Melissa Johnston for 3D printing required samples. This work utilized the Central Analytical Research Facility and Design & Fabrication Research Facility (DeFab) at the Queensland University of Technology (QUT).

Supplementary materials

Supplementary material associated with this article can be found, in the online version, at doi:10.1016/j.rineng.2025.107992.

Data availability

Data will be made available on request.

References

[1] S.-H. Lee, S. Yoo, S.H. Kim, Y.-M. Kim, S.I. Han, H. Lee, Nature-inspired surface modification strategies for implantable devices, Mater. Today Bio 31 (2025) 101615.

[2] S.P.S.N.B.S. Kumara, S.W.M.A.I. Senevirathne, A. Mathew, L. Bray, M. Mirkhalaf, P.K.D.V. Yarlagadda, Progress in nanostructured mechano-bactericidal polymeric surfaces for biomedical applications, Nanomaterials 13 (2023) 2799.

[3] M. Salta, L. Capretto, D. Carugo, J.A. Wharton, K.R. Stokes, Life under flow: a novel microfluidic device for the assessment of anti-biofilm technologies, Biomicrofluidics 7 (2013) 64118.

[4] E. Georgiades, C. Scianni, M.N. Tamburri, Biofilms associated with ship submerged surfaces: implications for ship biofouling management and the environment, Front. Mar. Sci. 10 (2023), https://doi.org/10.3389/fmars.2023.1197366.

[5] I. Pinel, R. Biškauskaitė, E. Pal'ová, H. Vrouwenvelder, M. van Loosdrecht, Assessment of the impact of temperature on biofilm composition with a laboratory heat exchanger module, Microorganisms 9 (2021) 1185.

[6] S. Jindal, S. Anand, L. Metzger, J. Amamcharla, Short communication: a comparison of biofilm development on stainless steel and modified-surface plate heat exchangers during a 17-h milk pasteurization run, J. Dairy Sci. 101 (2018) 2921–2926.

[7] L.M. Brown, J.P. McComb, M.D. Vangsness, L.L. Bowen, S.S. Mueller, L. M. Balster, C.A. Bleckmann, Community dynamics and phylogenetics of bacteria fouling Jet A and JP-8 aviation fuel, Int. Biodeterior. Biodegradation 64 (2010) 253–261.

[8] J. Gómez-Bolívar, M.P. Warburton, A.D. Mumford, J.F. Mujica-Alarcón, L. Anguilano, U. Onwukwe, J. Barnes, M. Chronopoulou, Y. Ju-Nam, S. F. Thornton, S.A. Rolfe, J.J. Ojeda, Spectroscopic and microscopic characterization of microbial biofouling on aircraft fuel tanks, Langmuir (2024), https://doi.org/10.1021/acs.langmuir.3c02803.

[9] D. Pruski, M. Sprynskyy, Jet fuel contamination: forms, impact, control, and prevention, Energies 17 (2024) 4267.

[10] J.S. Vrouwenvelder, D.A. Graf Von Der Schulenburg, J.C. Kruithof, M.L. Johns, M. C.M. Van Loosdrecht, Biofouling of spiralwound nanofiltration and reverse osmosis membranes: a feed spacer problem, Water Res. 43 (2009) 583–594.

[11] H. Chen, Z. Wei, G. Sun, H. Su, J. Liu, B. Hu, X. Zhou, L. Lou, Formation of biofilms from new pipelines at both ends of the drinking water distribution system and comparison of disinfection by-products formation potential, Environ. Res. 182 (2020) 109150.

[12] A. Mahapatra, N. Padhi, D. Mahapatra, M. Bhatt, D. Sahoo, S. Jena, D. Dash, N. Chayani, Study of biofilm in bacteria from water pipelines, J. Clin. Diagn. Res. 9 (2015) DC09–DC11.

[13] A.Y. Ganaraja, L. Mulky, Biofouling in industrial equipment: a look at quorum sensing and quorum quenching as anti-fouling strategies in membrane bioreactors, Environ. Technol. Rev. 13 (2024) 235–250.

[14] N.R. Maddela, A.S. Abiodun, S. Zhang, R. Prasad, Biofouling in membrane bioreactors-mitigation and current status: a review, Appl. Biochem. Biotechnol. 195 (2023) 5643–5668.

[15] E. Owusu, F.W. Asane, A.A. Bediako-Bowan, E. Afutu, Bacterial contamination of surgical instruments used at the surgery department of a major teaching hospital in a resource-limited country: an observational study, Diseases 10 (2022) 81.

[16] Y. Saito, H. Kobayashi, Y. Uetera, H. Yasuhara, T. Kajiura, T. Okubo, Microbial contamination of surgical instruments used for laparotomy, Am. J. Infect. Control 42 (2014) 43–47.

[17] B.R.H. Cervantes-Huamán, C. Ripolles-Avila, T. Mazaheri, J.J. Rodríguez-Jerez, Pathogenic mono-species biofilm formation on stainless steel surfaces: quantitative, qualitative, and compositional study, Lebenson. Wiss. Technol. 159 (2022) 113211.

[18] H. Julistiono, Y. Hidayati, N. Yuslaini, A. Nditasari, A. Dinoto, Sundjono, L. Nuraini, G. Priyotomo, H. Gunawan, Identification of biofilm-forming bacteria from steel panels exposed in sea waters of Jakarta Bay and Madura Strait, in: Author(s), 2018. https://doi.org/10.1063/1.5050125.

[19] S.W.M.A.I. Senevirathne, A. Mathew, Y.-C. Toh, P.K.D.V. Yarlagadda, Bactericidal efficacy of nanostructured surfaces increases under flow conditions, ACS Omega 7 (2022) 41711–41722.

[20] M. Ribeiro, F.J. Monteiro, M.P. Ferraz, Infection of orthopedic implants with emphasis on bacterial adhesion process and techniques used in studying bacterial-material interactions, Biomatter 2 (2012) 176–194.

[21] V.A.R. Barão, R.C. Costa, J.A. Shibli, M. Bertolini, J.G.S. Souza, Emerging titanium surface modifications: the war against polymicrobial infections on dental implants, Braz. Dent. J. 33 (2022) 1–12.

[22] N. Hossain, M.H. Mobarak, M.A. Islam, A. Hossain, M.Z. Al Mahmud, M. T. Rayhan, M.A. Chowdhury, Recent development of dental implant materials, synthesis process, and failure – a review, Results Chem. 6 (2023) 101136.

[23] S. Lin, H. Bi, C.E. Weinell, K. Dam-Johansen, Submerged surfaces exposed to marine biofouling – Experimental investigation of cleaning parameters effectiveness, Prog. Org. Coat. 172 (2022) 107097.

[24] F. Weber, N. Esmaeili, Marine biofouling and the role of biocidal coatings in balancing environmental impacts, Biofouling 39 (2023) 661–681.

[25] J.F. Mujica-Alarcon, J. Gomez-Bolivar, J. Barnes, M. Chronopoulou, J.J. Ojeda, S. F. Thornton, S.A. Rolfe, The influence of surface materials on microbial biofilm formation in aviation fuel systems, Biofouling 41 (2025) 265–282.

[26] K.J. Robinson, N.H. Voelcker, H. Thissen, Clinical challenges and opportunities related to the biological responses experienced by indwelling and implantable bioelectronic medical devices, Acta Biomater. 193 (2025) 49–64.

[27] Z. Khatoon, C.D. McTiernan, E.J. Suuronen, T.-F. Mah, E.I. Alarcon, Bacterial biofilm formation on implantable devices and approaches to its treatment and prevention, Heliyon 4 (2018) e01067.

[28] L. Kadirvelu, S.S. Sivaramalingam, D. Jothivel, D.D. Chithiraiselvan, D. Karaiyagowder Govindarajan, K. Kandaswamy, A review on antimicrobial strategies in mitigating biofilm-associated infections on medical implants, Curr. Res. Microb. Sci. 6 (2024) 100231.

[29] X. Chen, J. Zhou, Y. Qian, L. Zhao, Antibacterial coatings on orthopedic implants, Mater. Today Bio 19 (2023) 100586.

[30] Z. Sun, L. Ma, X. Sun, A.J. Sloan, N.M. O'Brien-Simpson, W. Li, The overview of antimicrobial peptide-coated implants against oral bacterial infections, Aggregate (2023), https://doi.org/10.1002/agt2.309.

[31] R.K. Roy, R. Biswas, A. Roy, R. Chandra, R. Shaw, A.K. Shaw, R. Bandopadhyay, Overview of the breadth of bacterial resistance development within the framework of antibiotics and antimicrobial peptides, Microbe 8 (2025) 100477.

[32] S.K. Ahmed, S. Hussein, K. Qurbani, R.H. Ibrahim, A. Fareeq, K.A. Mahmood, M. G. Mohamed, Antimicrobial resistance: impacts, challenges, and future prospects, J. Med. Surg. Public Health 2 (2024) 100081.

[33] Drug-Resistant Infections: A Threat to Our Economic Future, World Bank, Washington DC, 2017.

[34] P. Ebenezer, S.P.S.N.B.S. Kumara, S.W.M.A.I. Senevirathne, L.J. Bray, P. Wangchuk, A. Mathew, P.K.D.V. Yarlagadda, Advancements in antimicrobial surface coatings using metal/metaloxide nanoparticles, antibiotics, and phytochemicals, Nanomaterials 15 (2025) 1023.

[35] B. De Berardis, G. Civitelli, M. Condello, P. Lista, R. Pozzi, G. Arancia, S. Meschini, Exposure to ZnO nanoparticles induces oxidative stress and cytotoxicity in human colon carcinoma cells, Toxicol. Appl. Pharmacol. 246 (2010) 116–127.

[36] A.B. Sengul, E. Asmatulu, Toxicity of metal and metal oxide nanoparticles: a review, Environ. Chem. Lett. 18 (2020) 1659–1683.

[37] S. Mo, B. Mehrjou, K. Tang, H. Wang, K. Huo, A.M. Qasim, G. Wang, P.K. Chu, Dimensional-dependent antibacterial behavior on bioactive micro/nano polyetheretherketone (PEEK) arrays, Chem. Eng. J. 392 (2020) 123736.

[38] D. Patil, M. Overland, M. Stoller, K. Chatterjee, Bioinspired nanostructured bactericidal surfaces, Curr. Opin. Chem. Eng. 34 (2021) 100741.

[39] G. Hazell, L.E. Fisher, W.A. Murray, A.H. Nobbs, B. Su, Bioinspired bactericidal surfaces with polymer nanocone arrays, J. Colloid Interface Sci. 528 (2018) 389–399.

[40] E.P. Ivanova, J. Hasan, H.K. Webb, G. Gervinskas, S. Juodkazis, V.K. Truong, A.H. F. Wu, R.N. Lamb, V.A. Baulin, G.S. Watson, J.A. Watson, D.E. Mainwaring, R. J. Crawford, Bactericidal activity of black silicon, Nat. Commun. 4 (2013) 2838.

[41] E.P. Ivanova, D.P. Linklater, M. Werner, V.A. Baulin, X. Xu, N. Vrancken, S. Rubanov, E. Hanssen, J. Wandiyanto, V.K. Truong, A. Elbourne, S. Maclaughlin, S. Juodkazis, R.J. Crawford, The multi-faceted mechano-bactericidal mechanism of nanostructured surfaces, Proc. Natl. Acad. Sci. U.S.A. 117 (2020) 12598–12605.

[42] D.P. Linklater, V.A. Baulin, S. Juodkazis, R.J. Crawford, P. Stoodley, E.P. Ivanova, Mechano-bactericidal actions of nanostructured surfaces, Nat. Rev. Microbiol. 19 (2021) 8–22.

[43] T. Caykara, S. Fernandes, A. Braga, J. Rodrigues, L.R. Rodrigues, C.J. Silva, Can superhydrophobic PET surfaces prevent bacterial adhesion? Nanomaterials 13 (2023) 1117.

[44] D. Ashok, S. Cheeseman, Y. Wang, B. Funnell, S.-F. Leung, A. Tricoli, D. Nisbet, Superhydrophobic surfaces to combat bacterial surface colonization, Adv. Mater. Interfaces 10 (2023), https://doi.org/10.1002/admi.202300324.

[45] D. Patil, S. Aravindan, A. Pal, W.H. Khan, P. Pragya, S. Pundir, I. Xess, S. Mohapatra, V. Perumal, P.V. Rao, Microtopographic superhydrophobic polymer surface to prevent urinary tract infections causing nosocomial drug-resistant bacterial adhesion, Surf. Interfaces 41 (2023) 103239.

[46] S.V. Oopath, J. Martins, A.B. Kakarla, I. Kong, S. Petrovski, A. Baji, Rose petal mimetic surfaces with antibacterial properties produced using nanoimprint lithography, ACS Appl. Bio Mater. 6 (2023) 2690–2697.

[47] S. Miura, R. Yamagishi, N. Sugino, Y. Yokoyama, R. Miyazaki, K. Yasuda, M. Ando, Y. Hachikubo, T. Murashita, T. Kameda, Y. Kawano, S. Takei, Nanoimprint lithography and microinjection molding using gas-permeable hybrid mold for antibacterial nanostructures, J. Photopolym. Sci. Technol. 36 (2023) 183–190.

[48] S. Rowthu, P. Hoffmann, Versatile micro- and nanotexturing techniques for antibacterial applications. Functional Nanostructured Interfaces for Environmental and Biomedical Applications, Elsevier, 2019, pp. 27–62.

[49] S. Kim, U.T. Jung, S.-K. Kim, J.-H. Lee, H.S. Choi, C.-S. Kim, M.Y. Jeong, Nanostructured multifunctional surface with antireflective and antimicrobial characteristics, ACS Appl. Mater. Interfaces 7 (2015) 326–331.

[50] P.W. Doll, A. Al-Ahmad, A. Bacher, A. Muslija, R. Thelen, L. Hahn, R. Ahrens, B. Spindler, A.E. Guber, Fabrication of silicon nanopillar arrays by electron beam lithography and reactive ion etching for advanced bacterial adhesion studies, Mater. Res. Express 6 (2019) 065402.

[51] H. Shahali, J. Hasan, H. Wang, T. Tesfamichael, C. Yan, P.K.D.V. Yarlagadda, Evaluation of Particle Beam Lithography For Fabrication of Metallic Nano-Structures, 30, Procedia Manuf, 2019, pp. 261–267.

[52] G.-H. Ban, J. Lee, C.-H. Choi, Y. Li, S. Jun, Nano-patterned aluminum surface with oil-impregnation for improved antibacterial performance, Lebenson. Wiss. Technol. 84 (2017) 359–363.

[53] R.S. Sabry, A.H. Ali Al-fouadi, H.K. Habool, Enhanced antibacterial activity of anodic aluminum oxide membranes embedded with nano-silver-titanium dioxide, J. Adhes. Sci. Technol. 32 (2018) 874–888.

[54] A. Roy, K. Chatterjee, Bactericidal anisotropic nanostructures on titanium fabricated by maskless dry etching, ACS Appl. Nano Mater. 5 (2022) 4447–4461.

[55] M. Ganjian, K. Modaresifar, H. Zhang, P.-L. Hagedoorn, L.E. Fratila-Apachitei, A. A. Zadpoor, Reactive ion etching for fabrication of biofunctional titanium nanostructures, Sci. Rep. 9 (2019), https://doi.org/10.1038/s41598-019-55093-y.

[56] J. Hasan, Y. Xu, T. Yarlagadda, M. Schuetz, K. Spann, P.K. Yarlagadda, Antiviral and Antibacterial Nanostructured Surfaces with Excellent Mechanical Properties for Hospital Applications, ACS Biomater. Sci. Eng. 6 (2020) 3608–3618.

[57] N. Rawat, M. Benčina, E. Gongadze, I. Junkar, A. Iglič, Fabrication of antibacterial TiO_2 nanostructured surfaces using the hydrothermal method, ACS Omega 7 (2022) 47070–47077.

[58] A. Mathew, J. Hasan, S. Singamneni, P.K.D.V. Yarlagadda, Nanospikes on customized 3D-printed titanium implant surface inhibits bacterial colonization, Adv. Eng. Mater. 25 (2023), https://doi.org/10.1002/adem.202201306.

[59] Z.H. Ibupoto, K. Khun, M. Eriksson, M. AlSalhi, M. Atif, A. Ansari, M. Willander, Hydrothermal growth of vertically aligned ZnO nanorods using a biocomposite seed layer of ZnO nanoparticles, Materials 6 (2013) 3584–3597.

[60] A. Jaggessar, S.W.M.A.I. Senevirathne, A. Velic, P.K.D.V. Yarlagadda, Antibacterial activity of 3D versus 2D TiO2 nanostructured surfaces to investigate curvature and orientation effects, Curr. Opin. Biomed. Eng. 23 (2022) 100404.

[61] M.I. Ishak, R.C. Delint, X. Liu, W. Xu, P.M. Tsimbouri, A.H. Nobbs, M.J. Dalby, B. Su, Nanotextured titanium inhibits bacterial activity and supports cell growth on 2D and 3D substrate: a co-culture study, Biomater. Adv. 158 (2024) 213766.

[62] M. Maintz, C. Tourbier, M. de Wild, P.C. Cattin, M. Beyer, D. Seiler, P. Honigmann, N. Sharma, F.M. Thieringer, Patient-specific implants made of 3D printed bioresorbable polymers at the point-of-care: material, technology, and scope of surgical application, 3D Print. Med. 10 (2024) 13.

[63] G. Saponaro, M. Todaro, G. Barbera, G. Scivoletto, E. Foresta, G. Gasparini, A. Moro, Patient-specific facial implants in polyetheretherketone and their stability: a preliminary study, Ann. Plast. Surg. 90 (2023) 564–567.

[64] Z. Deng, Y. Wang, D. Zhang, C. Chen, 3D printing technology meets marine biofouling: a study on antifouling resin for protecting marine sensors, Addit. Manuf. 73 (2023) 103697.

[65] A.E. Wetzel, N. Del Castillo Iniesta, E. Engay, N.K. Mandsberg, C. Schou Dinesen, B.R. Hanif, K. Berg-Sørensen, A.-I. Bunea, R. Taboryski, Bioinspired microstructured polymer surfaces with antireflective properties, Nanomaterials 11 (2021) 2298.

[66] M.H. Mobarak, M.A. Islam, N. Hossain, M.Z. Al Mahmud, M.T. Rayhan, N. J. Nishi, M.A. Chowdhury, Recent advances of additive manufacturing in implant fabrication – a review, Appl. Surf. Sci. Adv. 18 (2023) 100462.

[67] Z. Wang, Y. Yang, Application of 3D printing in implantable medical devices, Biomed Res. Int. 2021 (2021) 6653967.

[68] A. Ariz, I. Tasneem, D. Bharti, A. Vaish, A. Haleem, M. Javaid, Is additive manufacturing of patient-specific implant beneficial for orthopedics, Apollo Med. 18 (2021) 33–40.

[69] X. Shi, V.A. Bobrin, Y. Yao, J. Zhang, N. Corrigan, C. Boyer, Designing nanostructured 3D printed materials by controlling macromolecular architecture, Angew. Chem. Int. Ed Engl. 61 (2022) e202206272.

[70] D. Patil, V. Golia, M. Overland, M. Stoller, K. Chatterjee, Mechanobactericidal nanotopography on nitrile surfaces toward antimicrobial protective gear, ACS Macro Lett. 12 (2023) 227–233.

[71] K. Yoo, W. Lee, K. Kang, I. Kim, D. Kang, D.K. Oh, M.C. Kim, H. Choi, K. Kim, M. Kim, J.D. Kim, I. Park, J.G. Ok, Low-temperature large-area fabrication of ZnO nanowires on flexible plastic substrates by solution-processible metal-seeded hydrothermal growth, Nano Converg. 7 (2020), https://doi.org/10.1186/s40580-020-00235-6.

[72] A. Jaggessar, A. Mathew, H. Wang, T. Tesfamichael, C. Yan, P.K. Yarlagadda, Mechanical, bactericidal and osteogenic behaviours of hydrothermally synthesised TiO2 nanowire arrays, J. Mech. Behav. Biomed. Mater. 80 (2018) 311–319.

[73] F. Tollini, S. Di Bartolo, G. Storti, M. Sponchioni, D. Moscatelli, Influence of pH and temperature on the kinetics of polylactic acid hydrolysis, Ind. Eng. Chem. Res. 64 (2025) 11733–11747.

[74] S.P.S.N Buddhika Sampath Kumara, S.W.M.A. Ishantha Senevirathne, Asha Mathew, Preetha Ebenezer, Tejasri Yarlagadda, Laura Bray, Mohammad Mirkhalaf, Prasad K.D.V. Yarlagadda, Nano-roughness modification of 3D printed Poly (lactic Acid) polymer via alkaline wet etching towards biomedical applications, J. Appl. Sci. Eng. 28 (2024) 1331–1340.

[75] M.S. Singhvi, S.S. Zinjarde, D.V. Gokhale, Polylactic acid: synthesis and biomedical applications, J. Appl. Microbiol. 127 (2019) 1612–1626.

[76] A.J.R. Barcena, P. Ravi, S. Kundu, K. Tappa, Emerging biomedical and clinical applications of 3D-printed poly(lactic acid)-based devices and delivery systems, Bioengineering 11 (2024) 705.

[77] F. Alam, V.R. Shukla, K.M. Varadarajan, S. Kumar, Microarchitected 3D printed polylactic acid (PLA) nanocomposite scaffolds for biomedical applications, J. Mech. Behav. Biomed. Mater. 103 (2020) 103576.

[78] C.B. de Souza Medeiros, B.L. Silva, A.M. Medeiros, J.D.D. Melo, A.P.C. Barbosa, Degradation of 3D-printed poly(lactic acid) for biomedical applications, Polym. Bull. (Berl.) 81 (2024) 6271–6281.

[79] S.W.M.A. Ishantha Senevirathne, P.K.D.V. Yarlagadda, The effect of the dual scale surface topography of a surface-modified titanium alloy on its bactericidal activity against *Pseudomonas aeruginosa*, RSC Adv. 15 (2025) 7209–7223.

[80] R. Giraud, V.-T. Ta, N. Papadakis, Evaluation framework of superpixel methods with a global regularity measure, J. Electron. Imaging 26 (2017) 061603.

[81] M. Schneider, N. Fritzsche, A. Puciul-Malinowska, A. Baliś, A. Mostafa, I. Bald, S. Zapotoczny, A. Taubert, Surface etching of 3D printed poly(lactic acid) with NaOH: a systematic approach, Polymers 12 (2020) 1711.

[82] C. Ma, Q. Guo, J. Mo, F. Lin, J. Chen, D. Cao, W. Xie, K. He, X. Liu, G. Xie, Y. Wu, Y. Zhang, J. Chen, Y. Wei, Monitoring and kinetic study of alkaline hydrolysis of polylactic acid fibrous membrane via aggregation-induced emission (AIE) technique, Surf. Interfaces 42 (2023) 103433.

[83] H. Tsuji, M. Ogiwara, S.K. Saha, T. Sakaki, Enzymatic, alkaline, and autocatalytic degradation of poly(l-lactic acid): effects of biaxial orientation, Biomacromolecules 7 (2006) 380–387.

[84] I. Grizzi, H. Garreau, S. Li, M. Vert, Hydrolytic degradation of devices based on poly(dl-lactic acid) size-dependence, Biomaterials 16 (1995) 305–311.

[85] H. Tsuji, K. Ikarashi, In vitro hydrolysis of poly(l-lactide) crystalline residues as extended-chain crystallites: II. Effects of hydrolysis temperature, Biomacromolecules 5 (2004) 1021–1028.

[86] H. Tsuji, Hydrolytic degradation, Poly(Lactic Acid) (2022) 467–516, https://doi.org/10.1002/9781119767480.ch21.

[87] C. Vasmara, G. Cazaudehore, E. Ceotto, R. Marchetti, C. Sambusiti, F. Monlau, Alkali, thermal, or thermo-alkali pre-treatment to improve the anaerobic digestion of poly(lactic acid)? Water Res. 258 (2024) 121744.

[88] D. Chauliac, P.C. Pullammanappallil, L.O. Ingram, K.T. Shanmugam, A combined thermochemical and microbial process for recycling polylactic acid polymer to optically pure L-lactic acid for reuse, J. Polym. Environ. 28 (2020) 1503–1512.

[89] A. Tarbuk, I. Čorak, D. Đorđević, Z. Draczyński, Accelerated hydrolysis of pla fibers at low temperature, (2022). https://doi.org/10.34658/9788366741751.55.

[90] M.Ranjbar Mohammadi, E. Naghashzargar, M. Kamali Moghaddam, R. Khorshidi, Production of PLA fibers with surface modifications and silver nanoparticle coating to impart antibacterial activity, Polym. Bull. 81 (2024) 6055–6072.

[91] G. Gorrasi, R. Pantani, Hydrolysis and biodegradation of poly(lactic acid). Synthesis, Structure and Properties of Poly(Lactic Acid), Springer International Publishing, Cham, 2017, pp. 119–151.

[92] W. Limsukon, M. Rubino, M. Rabnawaz, L.-T. Lim, R. Auras, Hydrolytic degradation of poly(lactic acid): unraveling correlations between temperature and the three phase structures, Polym. Degrad. Stab. 217 (2023) 110537.

[93] L. Song, Y. Li, X. Meng, T. Wang, Y. Shi, Y. Wang, S. Shi, L.-Z. Liu, Crystallization, structure and significantly improved mechanical properties of PLA/PPC blends compatibilized with PLA-PPC copolymers produced by reactions initiated with TBT or TDI, Polymers 13 (2021) 3245.

[94] B. Ma, X. Wang, Y. He, Z. Dong, X. Zhang, X. Chen, T. Liu, Effect of poly(lactic acid) crystallization on its mechanical and heat resistance performances, Polymer 212 (2021) 123280.

[95] Q. Zhou, M. Xanthos, Nanoclay and crystallinity effects on the hydrolytic degradation of polylactides, Polym. Degrad. Stab. 93 (2008) 1450–1459.

[96] A. Jimenez, M. Peltzer, R. Ruseckaite, Poly(lactic acid) science and technology: processing, properties, additives and applications. RSC Polymer Chemistry Series, Royal Society of Chemistry, 2015.

[97] Properties and Morphology of Poly(L-lactide) . II. Hydrolysis in alkaline solution, n.d.

[98] W.N. dos Santos, J.A. de Sousa, R. Gregorio Jr, Thermal conductivity behaviour of polymers around glass transition and crystalline melting temperatures, Polym. Test. 32 (2013) 987–994.

[99] N. Dhakal, X. Wang, C. Espejo, A. Morina, N. Emami, Impact of processing defects on microstructure, surface quality, and tribological performance in 3D printed polymers, J. Mater. Res. Technol. 23 (2023) 1252–1272.

[100] O.A. Mohamed, S.H. Masood, J.L. Bhowmik, Optimization of fused deposition modeling process parameters: a review of current research and future prospects, Adv. Manuf. 3 (2015) 42–53.

[101] M. El Mehtedi, P. Buonadonna, R. El Mohtadi, G. Loi, F. Aymerich, M. Carta, Optimizing milling parameters for enhanced machinability of 3D-printed materials: an analysis of PLA, PETG, and carbon-fiber-reinforced PETG, J. Manuf. Mater. Process. 8 (2024) 131.

[102] K. Erokhin, S. Naumov, V. Ananikov, Defects in 3D printing and strategies to enhance quality of FFF additive manufacturing. A review, ChemRxiv (2023), https://doi.org/10.26434/chemrxiv-2023-lw1ns.

[103] S. Deshmane, P. Kendre, H. Mahajan, S. Jain, Stereolithography 3D printing technology in pharmaceuticals: a review, Drug Dev. Ind. Pharm. 47 (2021) 1362–1372.

[104] T. Ma, Y. Zhang, K. Ruan, H. Guo, M. He, X. Shi, Y. Guo, J. Kong, J. Gu, Advances in 3D printing for polymer composites: a review, InfoMat 6 (2024), https://doi.org/10.1002/inf2.12568.

[105] R. Zhang, F. Du, K. Jariyavidyanont, E. Zhuravlev, C. Schick, R. Androsch, Glass transition temperature of poly(d,l-lactic acid) of different molar mass, Thermochim. Acta 718 (2022) 179387.

[106] O.C. Ibe, Introduction to descriptive statistics. Fundamentals of Applied Probability and Random Processes, Elsevier, 2014, pp. 253–274.

[107] J.A. Sánchez-García, L. Vázquez, R. Gago, A. Redondo-Cubero, J.M. Albella, Z. Czigány, Tuning the surface morphology in self-organized ion beam nanopatterning of Si(001) via metal incorporation: from holes to dots, Nanotechnology 19 (2008) 355306.

[108] W. Chen, Y. Wang, Y. Zhang, D. Yuan, Y. Yao, NaOH-catalyzed alcoholysis of polylactide, ACS Sustain. Chem. Eng. 13 (2025) 6771–6779.
[109] M.N. Siddiqui, L. Kolokotsiou, E. Vouvoudi, H.H. Redhwi, A.A. Al-Arfaj, D. S. Achilias, Depolymerization of PLA by phase transfer catalysed alkaline hydrolysis in a microwave reactor, J. Polym. Environ. 28 (2020) 1664–1672.
[110] H. Ito, Y. Tsutsumi, K. Minagawa, J. Takimoto, K. Koyama, Simulations of polymer crystallization under high pressure, Colloid Polym. Sci. 273 (1995) 811–815.
[111] V. Speranza, R. Salomone, R. Pantani, Effects of pressure and cooling rates on crystallization behavior and morphology of isotactic polypropylene, Crystals 13 (2023) 922.
[112] B.L.C. Cunha, J.O. Bahú, L.F. Xavier, S. Crivellin, S.D.A. de Souza, L. Lodi, A. L. Jardini, R.M. Filho, M.I.R.B. Schiavon, V.O.C. Concha, P. Severino, E.B. Souto, Lactide: production routes, properties, and applications, Bioengineering 9 (2022) 164.
[113] S.M. Weidner, F. Scheliga, H.R. Kricheldorf, Polycondensation, cyclization and disproportionation of solid Poly(L-lactide) trifluoroethyl esters and the simultaneous formation of extended chain crystals and extended ring crystals, Polymer 315 (2024) 127800.
[114] A. Theodorou, V. Raptis, C.I.M. Baltzaki, T. Manios, V. Harmandaris, K. Velonia, Synthesis and modeling of poly(L-lactic acid) via polycondensation of L-lactic acid, Polymers (2023) 15, https://doi.org/10.3390/polym15234569.
[115] Y. Maryanty, S. Hadiantoro, K. Widjajanti, D.I.K. Putri, L. Nikmah, Poly lactic acid (Pla) development using lactic acid product from rice straw fermentation with azeotropic polycondensation process, IOP Conf. Ser. Mater. Sci. Eng. 1053 (2021) 012043.
[116] H. Tsuji, Y. Ikada, Properties and morphology of poly(L-lactide). II. hydrolysis in alkaline solution, J. Polym. Sci. A Polym. Chem. 36 (1998) 59–66.
[117] S.-S. Park, Y.-S. Lee, S.-W. Lee, E. Repo, T.-H. Kim, Y. Park, Y. Hwang, Facile surface treatment of 3D-printed PLA filter for enhanced graphene oxide doping and effective removal of cationic dyes, Polymers 15 (2023) 269.
[118] T. Kimura, Natural products and biological activity of the pharmacologically active cauliflower mushroom Sparassis crispa, Biomed Res. Int. 2013 (2013) 982317.
[119] C.Y. Tham, Z.A.A. Hamid, Z.A. Ahmad, H. Ismail, Surface engineered poly(lactic acid) (PLA) microspheres by chemical treatment for drug delivery system, Key Eng. Mater. 594–595 (2013) 214–218.
[120] N. Ploypetchara, P. Suppakul, D. Atong, C. Pechyen, Blend of polypropylene/poly (lactic acid) for medical packaging application: physicochemical, thermal, mechanical, and barrier properties, Energy Procedia 56 (2014) 201–210.
[121] J. Xia, Y. Yuan, H. Wu, Y. Huang, D.A. Weitz, Decoupling the effects of nanopore size and surface roughness on the attachment, spreading and differentiation of bone marrow-derived stem cells, Biomaterials 248 (2020) 120014.
[122] S. Wu, F. Zuber, K. Maniura-Weber, J. Brugger, Q. Ren, Nanostructured surface topographies have an effect on bactericidal activity, J. Nanobiotechnol. 16 (2018), https://doi.org/10.1186/s12951-018-0347-0.
[123] H. Palza, B. Barraza, F. Olate-Moya, An overview for the design of antimicrobial polymers: from standard antibiotic-release systems to topographical and smart materials, Annu. Rev. Mater. Res. 52 (2022) 1–24.
[124] Developing antimicrobial polymeric nanostructured surfaces to combat biomaterial associated infections Ishak, M. I. (Author), 12 (2020).
[125] Songmei Wu, Flavia Zuber, Katharina Maniura-Weber, Juergen Brugger, Qun Ren, Nanostructured surface topographies have an effect on bactericidal activity, J. Nanobiotechnol. 16 (2018), https://doi.org/10.1186/s12951-018-0347-0.
[126] X. Zhang, J. Zhang, X. Han, S. Wang, L. Hao, C. Zhang, Y. Fan, J. Zhao, R. Jiang, L. Ren, A photothermal therapy enhanced mechano-bactericidal hybrid nanostructured surface, J. Colloid Interface Sci. 645 (2023) 380–390.
[127] Q. Cui, T. Liu, X. Li, K. Song, D. Ge, Nanopillared polycarbonate surfaces having variable feature parameters as bactericidal coatings, ACS Appl. Nano Mater. 3 (2020) 4599–4609.
[128] J. Jenkins, J. Mantell, C. Neal, A. Gholinia, P. Verkade, A.H. Nobbs, B. Su, Antibacterial effects of nanopillar surfaces are mediated by cell impedance, penetration and induction of oxidative stress, Nat. Commun. 11 (2020) 1626.
[129] A. Velic, A. Jaggessar, T. Tesfamichael, Z. Li, P.K.D.V. Yarlagadda, Effects of nanopillar size and spacing on mechanical perturbation and bactericidal killing efficiency, Nanomaterials 11 (2021) 2472.
[130] A. Velic, J. Hasan, Z. Li, P.K.D.V. Yarlagadda, Mechanics of bacterial interaction and death on nanopatterned surfaces, Biophys. J. 120 (2021) 217–231.
[131] L. Wang, V. Fogliano, J. Heising, M. Dekker, The effect of pore size on the diffusion of volatile antimicrobials is a key factor to preserve gelled foods, Food Chem. 351 (2021) 129316.
[132] R.H. Alasfar, S. Ahzi, N. Barth, V. Kochkodan, M. Khraisheh, M. Koç, A review on the modeling of the elastic modulus and yield stress of polymers and polymer nanocomposites: effect of temperature, loading rate and porosity, Polymers 14 (2022) 360.
[133] S. Teixeira, K.M. Eblagon, F. Miranda, M.F.R. Pereira, J.L. Figueiredo, Towards controlled degradation of poly(lactic) acid in technical applications, C 7 (2021) 42.